# Performance Analysis of the CALICE Digital Hadronic Calorimeter for Pion Measurements


*Yasmin Naghizadeh*

Department of Physics

McGill University

Montréal, Québec, Canada


August 14, 2024

A thesis presented for the degree of Masters of Physics

# Abstract

High-resolution, high-granularity calorimetry plays a crucial role in the advancement of modern particle detectors. These detectors are essential for precise measurements across a broad spectrum of physics phenomena, including the potential detection of dark matter and super symmetry particles. The CALICE international collaboration has developed scalable calorimeter prototypes to meet the demanding requirements of such detectors. One such prototype is the Digital Hadronic Calorimeter (DHCAL), optimized for event reconstruction using the Particle Flow algorithm. The cubic meter DHCAL consisting of about 500,000 of $1cm^2$ readout pads, has been tested extensively at Fermilab. Thanks to its imaging capabilities, the DHCAL with minimal absorber provides a powerful tool for detailed analysis of particle showers. This thesis presents the performance analysis of the DHCAL specifically for pion measurements, starting with event selection, particle identification, and calibration procedures. Experimental data in the energy range of 1 to 10 GeV is utilized, and results are compared with Monte Carlo simulations based on GEANT4 in order to improve the latter in this energy regime.

# Abrégé

La calorimétrie à haute résolution et haute granularité joue un rôle crucial dans l'avancement des détecteurs de particules modernes. Ces détecteurs sont essentiels pour des mesures précises dans un large éventail de phénomènes physiques, y compris la détection potentielle de la matière noire et des particules de supersymétrie. La collaboration internationale CALICE a développé des prototypes de calorimètres évolutifs pour répondre aux exigences rigoureuses de ces détecteurs. L'un de ces prototypes est le Calorimètre Hadronique Numérique (DHCAL), optimisé pour la reconstruction d'événements en utilisant l'algorithme Particle Flow. Le DHCAL d'un mètre cube, composé d'environ 500,000 pads de lecture de $1cm^2$, a été testé de manière extensive au Fermilab. Grâce à ses capacités d'imagerie, le DHCAL avec absorbeuses minimales fournit un outil puissant pour l'analyse détaillée des gerbes de particules. Cette thèse présente l'analyse de performance du DHCAL spécifiquement pour les mesures de pions, en commençant par la sélection des événements, l'identification des particules et les procédures de calibration. Des données expérimentales dans la gamme d'énergie de 1 à 10 GeV sont utilisées, et les résultats sont comparés avec des simulations Monte Carlo basées sur GEANT4 afin d'améliorer ces dernières dans ce régime d'énergie.

# Acknowledgements

I would like to thank my supervisor, François Corriveau, for his patience, and guidance and for giving me the opportunity to learn and work on a subject I am passionate about.

To my best friend, Asya Çiftci, thank you for your invaluable help and presence throughout this journey, and for investing your time in proofreading this thesis.

To William and my friends, Serena and Safeera, thank you for enduring my stress during the final stages of this thesis and encouraging me to keep working.

To the wonderful colleagues I met during my research and shared an office with, thank you for making my master's years enjoyable.

Lastly, to my Mom and Dad, without your support, love, and encouragement, I would not be able to be here.

# Contents

# List of Figures

# List of Tables

# List of Acronyms

**ASIC** Application-Specific Integrated Circuit.

**CALICE** Calorimeter for LInear Collider Experiment.

**DCAL** Digital Calorimetry chip.

**DHCAL** Digital Hadron Calorimeter.

**ECAL** Electromagnetic Calorimeter.

**FTBF** Fermilab Test Beam Facility.

**HCAL** Hadronic Calorimeter.

**HERA** Hadron-Electron Ring Accelerator.

**LEP** Large Electron-Positron Collider.

**LHC** Large Hadron Collider.

**Min-DHCAL** DHCAL with Minimal absorber.

**MIP** Minimum Ionising Particle.

**PFA** Particle Flow Alogtirthm.

**PID** Particle IDentification.

**pQCD** perturbative Quantum-ChromoDynamics.

**RPC** Resistive Plate Chamber.

**SiPM** Silicon Photomultiplier.

**SM** Standard Model of particle physics.

# Chapter 1

# Introduction

The discovery of elementary particles at the turn of the 20th century prompted the development of particle detection techniques and led to the development of the Standard Model of Particle Physics. Today, the high energy physics field continues to explore the fundamental components of matter through innovative experiments. High-granularity calorimeters, essential for implementing Particle Flow Algorithms used in jet energy reconstruction, are developed by CALICE collaboration, for this purpose. This thesis focuses on the Digital Hadronic Calorimeter (DHCAL) with a minimal absorber, which underwent testing in several test beams at Fermilab in 2011.

In Chapter 2, an overview of the standard Model and its extensions beyond the current theory will be provided. Chapter 3 will discuss the different ways particles interact with matter, covering topics such as energy loss of charged particles, Cherenkov radiation, photon interaction, and both hadronic and electromagnetic showers.

Chapter 4 will introduce the fundamental aspects of calorimeters, including their resolution and the principles behind imaging calorimeters and particle flow algorithms. It will also discuss the clustering algorithm used in this analysis. The experimental setup, focusing on the CALICE detector, and the test beam setups, will be detailed in Chapter 5. This chapter will highlight the Digital Hadronic Calorimeter (DHCAL) and its configuration with minimal absorber (Min-DHCAL), as well as the Fermilab test beam setup.

Chapter 6 will cover the analysis of the collected data, detailing the run parameters, event selection processes, and particle identification methods. It will also discuss calibration techniques with the Min-DHCAL and Monte Carlo simulations.

The results of the study will be presented in Chapter 7, including the response to pions, longitudinal and lateral shower profiles, hit density distributions, and concluding with a comprehensive estimate of the systematic errors.

Finally, Chapter 8 will offer a discussion of the findings and provide concluding remarks on the research, summarizing the insights gained and their implications for future work in the field. This will complete the first such investigation on positrons, following the study conducted in 2015 [1].

# Chapter 2

# Theory

## 2.1 The Standard Model

Since the 1890s and the discovery of electrons by Thomson [2], followed by the discovery of the nucleus by Rutherford in 1911 [3] and the discovery of the neutron by Chadwick in 1932 [4], the atomic model was deemed complete. The atomic model prompted physicists to question, “What holds the nucleus together?”. This was first addressed by Yukawa in 1934 with the introduction of the strong force theory. Yukawa predicted the existence of a particle, now known as a meson, with a mass between that of an electron and a proton, which would mediate the strong force binding the nucleus. In particle classification, lighter particles like the electron are called leptons, while heavier ones like the proton and neutron are categorized as baryons. The identification of mesons, baryons, and leptons, along with the discovery of quarks and the development of theories to explain their interactions, led to the emergence of a theory describing the interaction of all known forces, except gravity, in the 1960s and 1970s. This collective framework relating families of elementary particles, incorporating quantum electrodynamics, the Glashow-Weinberg Salam theory of electroweak interactions, and quantum chromodynamics is referred to as the Standard Model [5].

The fundamental particles of the Standard Model are fermions and bosons. The fundamental forces of the Standard Model have bosons with integer spin, as the force mediator particles. The photon is the force mediator of the electromagnetic force; $W^{\pm}$, and $Z^0$ are the electroweak force's mediators; the gluons are the mediators of the strong force, and the most recent experimentally confirmed boson is the Higgs with spin zero. Quarks and leptons, subdivisions of fermions, with half-integer spins, interact with each other by exchanging bosons. Color-charged quarks interact primarily through strong force by exchanging gluons as the color charge carriers in red, green, and blue. However, they can interact through other bosons with other forces as well. Charged leptons interact electromagnetically by exchanging photons and they also interact through the weak force.

Figure 2.1 shows the classification of elementary particles through the Standard Model. Three generations of fermions, couple to the bosons. There are six known leptons: the

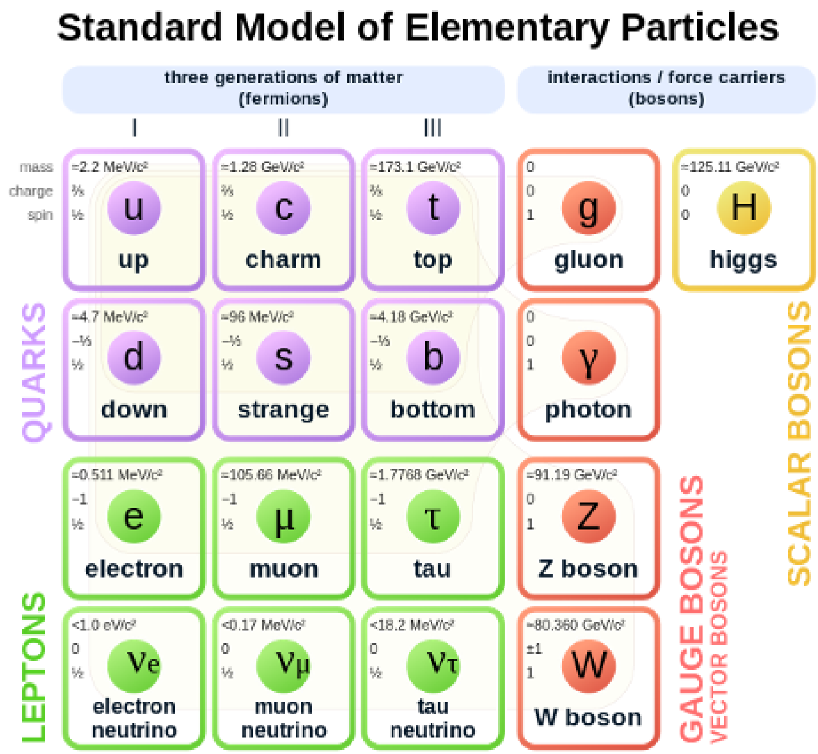


**Figure 2.1:** Standard Model of Elementary Particles. Three generations of quarks and leptons are separated based on their masses, from the lightest in I, to the heaviest in III. Masses, spins, and charges in units of e for each particle are indicated. [6]

electron $e$, the muon $\mu$, the tau $t$, and the three associated neutrinos. Neutrinos being very light with no charge only interact through the weak force and gravity. There are six known quarks: the up $u$, the down $d$, the strange $s$, the bottom $b$, the top $t$, and the charm $c$. All elementary particles listed in the Standard Model in Figure 2.1, have a corresponding antiparticle. Antiparticles carry the same mass and spin as the particles, but with the opposite charge sign.

## 2.2 Beyond the Standard Model

While the Standard Model has been successful in describing the interaction of the fundamental particles at the subatomic level and all particles of the Standard Model have been observed through experiments, it still has some shortcomings. Above all, although all massive particles experience gravitational interactions, gravity is extremely weak, approximately 34 orders of magnitude weaker than other forces at the subatomic level. Therefore, gravity is not included in the Standard Model of particle physics [7]. Additionally, the Standard Model, which incorporates the Higgs mechanism as formulated by Steven Weinberg and Abdus Salam to describe how particle masses are generated, does not account for the experimentally observed oscillations of neutrinos. Notably, while the Higgs mechanism is essential in explaining the masses of other particles, the Standard Model does not account for neutrino masses [8]. Furthermore, the matter explained by the Standard Model accounts for only about 5% of the universe, while about 26% consists of dark matter and more than 68% of the universe is composed of dark energy, neither of which is explained by the Standard Model [9]. All these shortcomings of the Standard Model have raised the need to build new particle experiments to investigate these open questions. The design of new particle accelerators and new collider complexes requires the development of new detector concepts with wide energy ranges, improved timing, enhanced energy and statistical resolution, and faster devices to meet these requirements.

# Chapter 3

# Particle Interaction with Matter

In particle physics, an ‘event’ is the outcome of a particle collision between high-energy particles, and ‘reconstruction’ refers to determining the properties of the particles involved. To effectively reconstruct events, it is essential to know the energy of individual particles in a collision. Experimental techniques are employed to identify particles and their properties through their interactions with matter. Therefore, comprehending the processes of particle interaction is crucial for developing detector techniques and correcting data for particle detectors.

## 3.1 Energy Loss of Charged Particles

Charged particles interact predominantly by electromagnetic interactions. Deflection from the initial direction of the particle through collision and the particle’s energy loss are the two core concepts featuring the interaction of charged particles with matter [10]. This section will concentrate on the three most common energy loss processes: Ionization/Excitation, Bremsstrahlung, and Cherenkov Radiation.

### 3.1.1 Energy Loss in matter

Charged particles traversing a material interact either by exciting or ionizing the atoms within the material. During these interactions, these charged particles lose kinetic energy by emitting low-energy photons, which can be captured by detectors that record the resulting luminescence. The average energy loss ($dE$) per length ($dx$) through excitation or ionization of heavy charged particles is approximated using Beth and Bloch Formula 3.1 [11]:

$$-\frac{dE}{dx} = 4\pi N_A r_e^2 m_e c^2 z^2 \frac{Z}{A}\frac{1}{\beta^2}(ln\frac{2m_e c^2\gamma^2\beta^2}{I} - \beta^2 - \frac{\sigma}{2})[\frac{MeV}{(g/cm^2)}], \tag{3.1}$$

where:

$z$- incident particle's charge

$Z$- the atomic number of the absorber material

$A$- the atomic weight of the absorber material

$m_e$- electron mass

$r_e$- classical electron radius

$N_A$- Avogadro number

$I$ – mean excitation energy of the absorber material

$\sigma$- density correction factor

$\gamma$- Lorentz factor

As seen from Equation 3.1, the energy loss of the particles is mass-independent, and it only depends on the charge and velocity of the incoming particle. It is accurate up to a few percent for energies of a few hundred GeV. As shown in Figure 3.1, the Bethe-Bloch formula is plotted for different particles and materials as a function of kinetic energy:
As seen in Figure 3.1, the mean energy loss given by the Bethe-Bloch formula follows the same trend for different materials, where the energy of the non-relativistic low energy range decreases, dominating by $\frac{1}{\beta^2}$ until reaching a minimum. Particles that lose energy corresponding to this minimum are called Minimum Ionizing Particles (MIP). This minimum in loss of energy is followed by a so-called relativistic rise. However, this formula is accurate for heavy particles. Electrons as the incident particles require a more exact formula since electrons as incident particles have the same mass as the target electrons, and since the Bremsstrahlung processes influence electrons. Equation 3.2 considers the electron-electron collisions and the screening effects for electrons [11].

$$-\frac{dE}{dx} = 4\pi N_A r_e^2 m_e c^2 \frac{Z}{A}.\frac{1}{\beta^2}[ln\frac{\gamma m_e c^2\sqrt{\gamma-1}}{\sqrt{2}I} + \frac{1}{2}(1-\beta^2) - \frac{2\gamma-1}{2\gamma^2}ln2 + \frac{1}{16}(\frac{\gamma-1}{\gamma})^2] \quad (3.2)$$

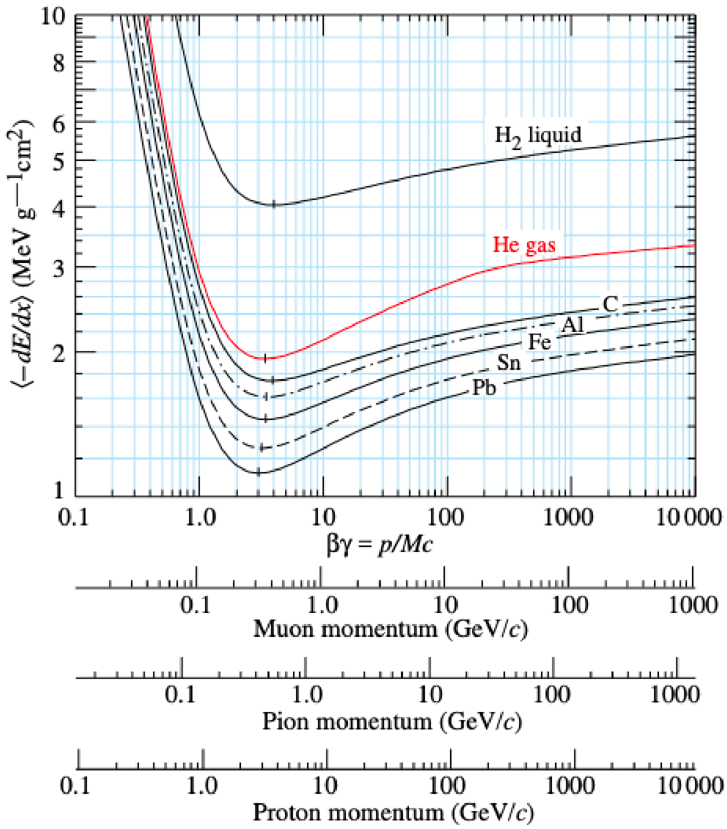


**Figure 3.1:** Mean energy loss ($dE$) per length ($dx$) in liquid hydrogen, helium gas, carbon, aluminum, iron, tin, and lead for muon, pion, and proton. [12]

As the energy of incoming particles rises, the key process of energy loss transitions from Ionization/Excitation to Bremsstrahlung.

### 3.1.2 Bremsstrahlung

By interacting with the Coulomb field of the nuclei in the medium being traversed, fast charged particles lose energy. Their kinetic energy will be emitted as photons through the process of bremsstrahlung when they are decelerated and/or deflected. Equation 3.3 describes the energy loss by bremsstrahlung for high energy particles:

$$-\frac{dE}{dx} \approx 4\alpha N_A \frac{Z^2}{A} z^2 (\frac{1}{4\pi\epsilon_0}\frac{e^2}{mc^2})^2 E ln \frac{183}{Z^{1/3}}, \tag{3.3}$$

where:

$Z$- atomic number of the medium

$A$- atomic weight of the medium

$z$- charge number of the incident particle

$m$- mass of the incident particle

$E$- energy of the incident particle

Bremsstrahlung energy losses play a particularly significant role due to the relatively small mass of the electron and can be written as:

$$-\frac{dE}{dx} = \frac{E}{X_0} \tag{3.4}$$

The radiation length $X_0$ is described in this Equation 3.5 as:

$$X_0 = \frac{A}{4\alpha N_A Z(Z+1) r_e^2 ln(183 Z^{-1/3})} [\frac{g}{cm^2}], \tag{3.5}$$

where:

Z- atomic number of the absorber material

A- atomic weight of the absorber material

Radiation length represents the mean distance over which high-energy electrons, through the process of bremsstrahlung, lose all but 1/e of their energy. Radiation length is a valuable metric for measuring the thickness of various materials because the energy loss can be expressed independently of the absorber material. Equation 3.6 characterizes the exponential attenuation of the charged particles' energy due to the bremsstrahlung energy losses [11]:

$$E = E_0 e^{-x/X_0} \tag{3.6}$$

The energy at which both the Bremsstrahlung and ionization result in equal energy losses is referred to as the critical energy. As seen from Figure 3.2, for an electron or positron the energy loss at low energies is dominated by the ionization process, and after intersecting with Bremsstrahlung at the critical energy point, Bremsstrahlung dominates at high energies.

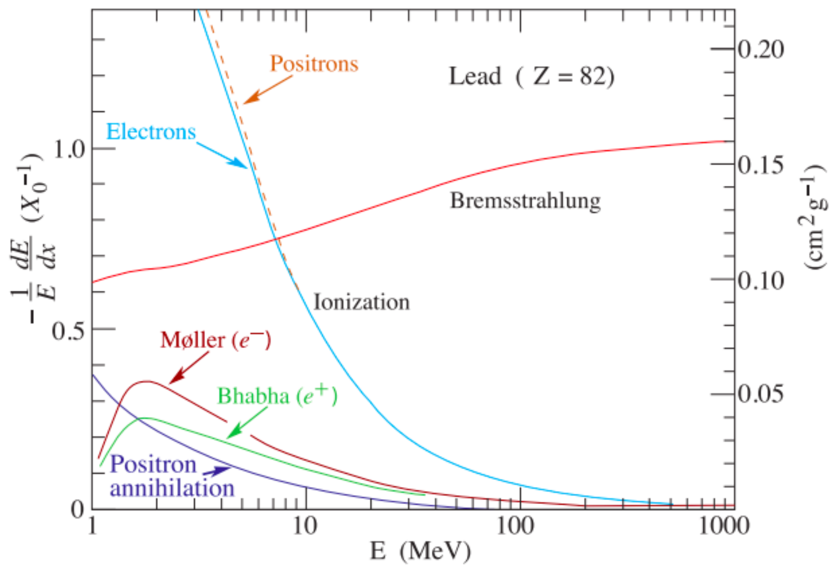


**Figure 3.2:** Fractional energy loss of electron or positron traveling through lead. [12]

### 3.1.3 Electron-Pair Production

At high energies, virtual photons in the Coulomb field of the nuclei can be transformed into electron-positron pairs. This energy loss plays a more important role than Bremsstrahlung energy losses for heavier particles. This energy loss can be parametrized by [11]:

$$\frac{dE}{dx}|_{pairpr.} = b_{pair}(Z, A, E).E \tag{3.7}$$

The $b_{pair}$ is proportional to energy and varies slowly with energy. Effective values for A and Z are calculated as:

$$A_{eff} = \sum_{i=1}^{N} f_i A_i, \tag{3.8}$$

$$Z_{eff}.(Z_{eff}+1) = \sum_{i=1}^{N} f_i Z_i(Z_i+1), \tag{3.9}$$

where $f_i$ is the mass fraction, $A_i$ is the atomic weight, and $Z_i$ is the charge number. For detailed information on radiation lengths and critical energies for different absorber materials, refer to [11].

## 3.2 Cherenkov Radiaion

When a particle propagating through a medium exceeds the speed of light in that same medium, the medium through which it is traveling emits Cherenkov radiation. This particle will have the following velocity:

$$v_{particle} > c/n, \tag{3.10}$$

where $n$ is the refraction index and $c$ is the speed of light in the vacuum. Using Equation 3.11, the energy loss can be calculated as:

$$-\frac{dE}{dx} = z^2 \frac{\alpha\hbar}{c} \int \omega d\omega sin^2\theta_c = z^2 \frac{\alpha\hbar}{c} \int \omega d\omega (1 - \frac{1}{\beta^2 n^2(\omega)}), \tag{3.11}$$

where $\alpha$ represents the fine structure constant, $z$ is the charge of the particle, $\hbar$ is the reduced Planck's constant, $\omega$ is the angular frequency of the radiation, $\theta_c$ is the Cherenkov angle, and $\beta$ is the particle's velocity as a fraction of the speed of light, with which the energy loss increases. Particle physicists exploit Cherenkov radiation in the Cherenkov counter, where it is detected using photomultipliers by converting photons into electrical current pulses to count their number [10]. The number of photons emitted per unit frequency per unit length of radiator can be calculated using Equation 3.12:

$$\frac{d^2N}{d\omega dx} = \frac{z^2\alpha}{c} sin^2\theta_c = \frac{z^2\alpha}{c}(1 - \frac{1}{\beta^2 n^2(\omega)}) \tag{3.12}$$

## 3.3 Interaction of Photons

Photons are detected indirectly in a detector through the generation of charged particles, which ionize the active medium of the detector and are subsequently recorded. Due to photons' lack of electric charge, their interaction with the medium of the detector is fundamentally different from charged particles. Photons are either scattered via the Compton effect or they are completely absorbed through the photoelectric or pair production effects. It is impossible to define a range for photons as they interact through these statistical processes.

A photon beam attenuates exponentially as it passes through matter according to:

$$I = I_0 e^{-\mu x}, \tag{3.13}$$

where $\mu$ is the mass attenuation coefficient, and it is related to the cross-section of the photon's various interaction processes.

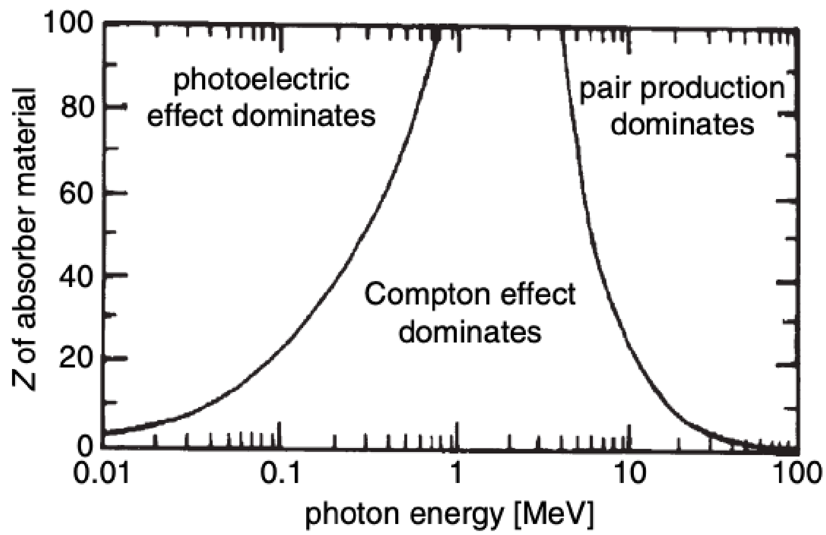


**Figure 3.3:** Domination range of photoelectric, the Compton effect, and pair production as a function of the photon energy and the absorber's charge number $Z$. [11]

As seen in Figure 3.3, the photoelectric effect dominates at lower energies, the Compton effect dominates for medium-range energies, and pair production dominates at higher energies.

## 3.4 Hadronic Interactions

Similar to electromagnetic interactions, explained in previous sections, hadrons undergo inelastic interactions, resulting in the production of secondary particles during collisions [11]. To describe the absorption-like losses of hadrons, similar to those for electrons, the average interaction length denoted as $\lambda_I$, is used according to 3.14:

$$N = N_0 e^{-x/\lambda_I} \tag{3.14}$$

The inelastic part of the hadronic cross-section is used to calculate $\lambda_I$ as 3.15:

$$\lambda_I = \frac{A}{N_A \varrho \sigma_{inel}} [cm], \tag{3.15}$$

where:

- $\varrho$ : density in units of $g/cm^3$

- A: the atomic mass of the absorber

- $\sigma_{inel}$: inelastic cross section in $cm^2$

- $N_A$: Avogadro's number

## 3.5 Electromagnetic Showers

The following simplified sketch describes the electromagnetic shower model in Figure 3.4. According to this model, an incident photon with energy $E_0$ after one radiation length $X_0$ through the detector will produce an $e^+e^-$ pair. Each electron and positron will produce one Bremsstrahlung photon after another radiation length, which each produces another

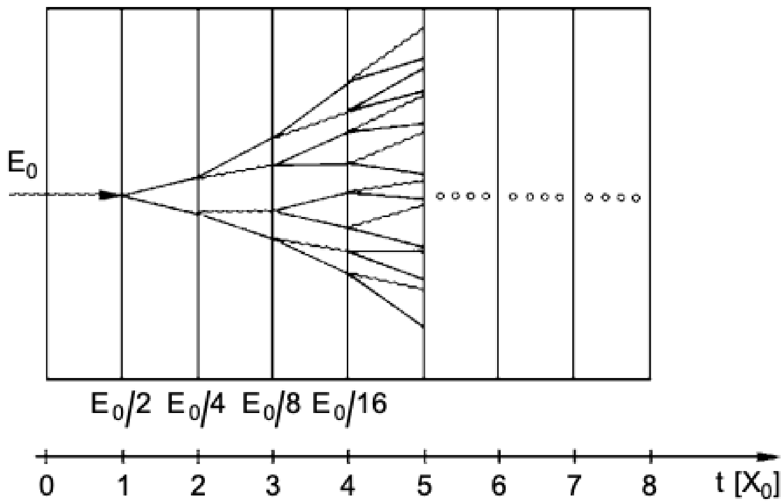


**Figure 3.4:** Simplified electromagnetic shower model. $t$ is the depth (in $X_0$ units). [11]

electron-positron pair. Assuming the energy is symmetrically shared at each step between particles, the number of particles at depth $t$ can be calculated by Equation 3.16:

$$N(t) = 2^t \tag{3.16}$$

Particle's average energies can be calculated by Equation 3.17:

$$E(t) = E_0 2^{-t} \tag{3.17}$$

The position of the shower maximum in this model is calculated by Equation 3.18:

$$E_c = E_0.2^{-t_{max}} \tag{3.18}$$

This simplified model can correctly describe the characteristics of an electromagnetic shower:

- To completely absorb the incident photon's energy, calorimeters require a thickness of more than $2X_0$.
- The calorimeter's thickness, logarithmically depends on the energy since the position of the shower maximum increases with energy.
- Most leakage is caused by soft photons escaping through the back of the detector.

The shower maximum location, representing the distance at which each particle's energy reaches the critical energy, can be calculated using Equation 3.18.

$$t_{max} = \frac{ln(E_0/E_c)}{ln(2)} \tag{3.19}$$

Electromagnetic lateral width is primarily influenced by multiple scattering and best described by the Moliere radius, Equation 3.20:

$$R_M = \frac{21MeV}{E_c} X_0[g/cm^2] \tag{3.20}$$

By increasing the longitudinal shower depth, the electromagnetic shower's lateral width is increased.

## 3.6 Hadronic Showers

Hadronic showers are characterized by the production of a cascade of secondary particles when hadrons interact inelastically. Currently, there is no comprehensive theory detailing hadronic showers, as they are significantly more complex than that of electromagnetic showers. Nuclear interaction length $\lambda_I$ is used to quantify the longitudinal progression of a hadronic shower, which is typically much larger than the radiation length $X_0$. Consequently, in order to accommodate the extended longitudinal development of hadronic showers, hadronic calorimeters must be considerably thicker than electromagnetic calorimeters.

In addition to their greater longitudinal extension, hadronic showers have a narrow lateral distribution initially, but it widens with increasing depth within the detector. The lateral size of hadronic showers is dominated by large transverse energy transfers during nuclear interactions.

As the average particle multiplicity in hadronic showers increases logarithmically with energy, the number of secondary particles, including neutral pions, also rises. Most of these neutral pions, with a decay time on the order of $10^{-17}$ seconds, decay electromagnetically into photons, initiating electromagnetic subshowers within the hadronic shower.

One of the key challenges in detecting hadronic showers, as it is expended in breaking nuclear bonds, is that a substantial fraction of the energy remains invisible. As a result, in a calorimeter, the signal from a hadron is generally smaller than that from an electron. Calorimeters that are designed to equalize the ratio of electromagnetic to hadronic response ($\frac{e}{h}$) can partially recover the invisible energy and are termed compensating calorimeters. Compensating calorimeters provide a more precise measurement of the hadronic shower energy.

# Chapter 4

# Calorimeters

Calorimeters are instruments designed to convert the absorbed energy of the particles interacting into a measurable signal. Incident particles interact through electromagnetic or strong interactions with the detector and generate a shower of secondary particles. The deposited energy is measured as charge or light, providing a measurement of the incident particle's energy.

Calorimetry has become an essential detection technique in high-energy physics, evolving from its origins in cosmic-ray research to address the sophisticated demands of modern particle physics experiments. Calorimeters offer high energy resolution, improving with the square root of the energy ($\propto 1/\sqrt{E}$). Unlike magnetic spectrometers, they can detect all particle types, including neutral particles, and interpret neutrino presence by measuring missing energy. Their versatility extends to particle trajectory determination, particle identification, and rapid signal processing for triggering [13]. These features have made calorimeters crucial in major experiments at facilities like the Large Electron-Positron Collider (LEP), the Hadron-Electron Ring Accelerator (HERA), the Tevatron at Fermilab, and the Large Hadron Collider (LHC). For instance, LEP used electromagnetic calorimeters with lead glass and silicon-tungsten detectors, while HERA used calorimeters of two types: liquid argon with steel absorber or plastic scintillators with uranium plates. The Tevatron utilized a hybrid system combining scintillating materials and iron for accurate energy measurements. These advancements in calorimetry continue to drive exploration in particle physics, from precision measurements to new particle discoveries

## 4.1 Type of Calorimeters

Calorimeters are classified into two main types based on the particles they measure: electromagnetic calorimeters and hadronic calorimeters. Furthermore, they are classified based on their construction: sampling calorimeters and homogeneous calorimeters. Sampling calorimeters are composed of alternating layers of an absorber and an active medium. An absorber is used to degrade the energy of the incident particle, and an active medium is used to generate the detectable signal. Homogeneous calorimeters are composed of a single type of layer that simultaneously degrades the particle's energy and produces the detectable signal [13]. Sampling calorimeters, by sampling the energy, are much more compact, making them better suited for high-energy experiments where a larger detector volume would be impractical.

## 4.2 Resolution

Energy resolution measures how precisely the energy of a given particle can be determined; therefore, it is typically the primary goal of calorimeters to achieve the best possible energy resolution for particles. The resolution is commonly approximated using the following parametrization [11]:

$$\frac{\sigma_E}{E} = \frac{a}{\sqrt{E}} \oplus \frac{b}{E} \oplus c, \tag{4.1}$$

where:

- $a$: main stochastic term

- $b$: instrumental's error factor, such as dead areas (refer to section 6.1)

- $c$: calibration uncertainties constant, such as the electronic noise

- $\oplus$: quadrature summation

## 4.3 Imaging Calorimeter

Imaging calorimeters are generally sampling calorimeters based on fine segmentation of the readout, resulting in a large number of readout channels. Additionally, the front-end electronics must be positioned on the surface of the active medium, embedding them into the calorimeter structure [14]. Resistive Plate Chambers (RPC), silicon wafers, scintillator strips, Gas Electron Multipliers, and Micromegas are among the many possible candidates for the active medium of an imaging calorimeter.

The primary advantage of imaging calorimeters is applying the Particle Flow Algorithm (PFA) (see section 4.3). Additionally, highly segmented imaging calorimeters enhance the precision measurement of individual hadronic jets with high resolution. Moreover, in multijet events, the resolution of dijet masses, the invariant mass calculated from the combined four-momenta of the two jets when it comes from the decay of some particle or resonant state, is improved by facilitating the assignment of calorimeter energy deposited into the respective jets.

Another advantage of an imaging calorimeter is that its fine segmentation makes it possible to distinguish electromagnetic sub-showers within a hadronic shower, which allows for the implementation of software compensation techniques. This capability allows exhibiting an electron-to-hadron ratio (e/h), the relative response to electromagnetic versus hadronic showers, close to unity, and as a result, enhances the energy resolution of hadrons by approximately 20% [15].

When particles are not completely stopped in the detector, it causes leakage, which as a result degrades the energy resolution. By using detailed longitudinal and lateral showers, imaging calorimeters can correct for the leakage and therefore improve the energy resolution and provide valuable insight into the shape of the hadronic showers.

## 4.4 Particle Flow Algorithm

For advanced particle physics experiments, the concept of high-granularity Particle Flow calorimetry has to be developed. This approach is designed to characterize physics processes that result in multi-jet final states, often accompanied by single particles and/or missing transverse energy due to neutrons or the lightest super-symmetric particles. The invariant masses of two or more jets reconstruction offers a powerful method for both event reconstruction and event identification. In the traditional calorimetric method, the energy of a jet is obtained by summing the energies deposited in the electromagnetic calorimeter (ECAL) and the hadronic calorimeter (HCAL). This approach typically results in a jet energy resolution in the form of Equation 4.1 where the stochastic term, $a$, of a hadronic calorimeter, is about 60% and the constant term $c$ is a few percent. For high-energy jets, the shower leakage of hadronic showers will also have a contribution.

These calorimeters process imaging capabilities comparable to those of the tracker, requiring the reconstruction of four vectors, for the most visible particles in an event. By summing the individual energies of these particles, the jet energy can be reconstructed. Photon energy is measured in the ECAL, and the energy of neutral hadrons is primarily measured in the HCAL. PFA combines tracking techniques with the energy measurements from the calorimeters, achieving an improved jet energy resolution of $3 - 4\%$ by utilizing complex pattern recognition software, such as the Pandora PFA, for event reconstruction [16].

## 4.5 Clustering

By associating hits with distinct particles within a single event, clustering plays a crucial role in imaging calorimetry for implementing software compensation and identifying particles, but also for calibration purposes. In this analysis, a nearest neighbor algorithm is employed, wherein hits that share a common side are grouped in the same cluster. To provide spatial information, the mean x and mean y positions are computed for each cluster. This approach enhances the precision of particle tracking and energy measurement. Figure 4.1 shows a schema of the clustering algorithm.

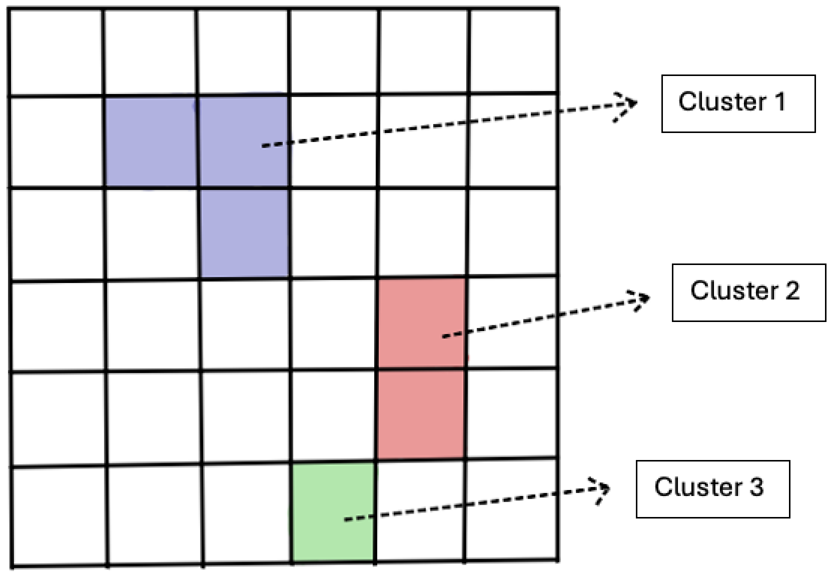


**Figure 4.1:** The first cluster has 3 hits with common sides, the second cluster has 2 hits with common sides, and the third cluster has only one hit.

# Chapter 5

# Calice Detector and Test Beam Setup

The CAlorimeter for LInear Collider Experiment (CALICE) collaboration [17] has been developing new detector technologies to achieve high-precision measurements for high-energy physics experiments. The high granular detectors are designed for high lateral and longitudinal segmentation and are optimized for the PFA. CALICE has developed several electromagnetic and hadronic calorimeters with either steel or tungsten as the absorber layers using various detection methods, including, scintillators, silicon, and gas. The main characteristic of the Digital Hadronic Calorimeter (DHCAL) developed by CALICE will be explained in the following section as the main subject of this thesis.

## 5.1 Digital Hadronic Calorimeter

The Digital Hadronic Calorimeter, developed by CALICE collaboration, is a PFA-optimized calorimeter based on Resistive Plate Chambers (RPC) as active elements. The DHCAL prototype was constructed during the 2008-2010 period and later underwent evaluation using the test beams at Fermilab and CERN [18–20]. The digital readout records only the hits rather than the actual energy deposited, which causes saturation effects (see section 7.1.2). This limitation results in a diminished energy resolution at higher energy levels. On the other hand, the cost-effectiveness of RPC technologies and simpler calibration procedures of digital readout systems compared to those required for Silicon Photomultiplier (SiPM) offer significant benefits, making them a cost-efficient option for precision measurements.

### 5.1.1 RPC Design

Resistive Plate Chambers (RPCs) are characterized by their straightforward and robust design, as well as their low noise levels, reliability, and cost-effectiveness in construction. The readout system of RPCs can be segmented and tailored to meet the specific demands of finely granulated hadron calorimeters [21]. In general, RPCs utilize glass for the resistive plates, across which a high voltage of 6-7 kV, is applied over a gas-filled gap. A charged particle traversing this gap causes ionization. The resulting ionized particles are then further multiplied by an avalanche effect. This amplified signal then propagates across the resistive plate to the anode, where it induces a charge on the readout board. RPCs can function in either streamer mode or avalanche mode. Although, for the DHCAL, an avalanche design demands more precise control over the plate resistivity, it is more suitable due to its compatibility with the one-bit readout design [22].

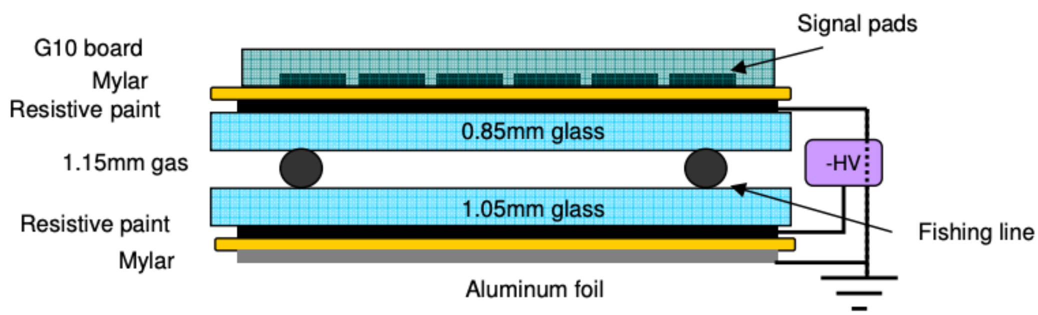


**Figure 5.1:** RPCs used in the design of DHCAL [23].

Each layer of DHCAL consists of three $32 \times 96$ $cm^2$ RPCs, each with 1 $cm^2$ readout cells, resulting in a total active area of $96 \times 96$ $cm^2$ for each layer. As shown in Figure 5.1, the two soda-lime glasses are separated by a 1.15 $mm$ gas gap. The 0.85 $mm$ glass on the anode is designed thinner than the cathode, 1.15 $mm$, to reduce the average pad multiplicity by maintaining the average number of active pads at approximately one, by minimizing the distance between the gas gap and the anode. To facilitate uniform gas flow throughout the chamber, the two resistive plates are separated by fishing lines spaced 5 cm apart [22, 24]. The inflammable gas mixture contains 94.5% tetrafluroethene, 5% isobutane, and 0.5% sulfurhexafluoride.

An alternative configuration to the standard 2-glass RPC design is utilizing a single soda lime glass which has been evaluated and demonstrates promising performance. This single-glass design offers benefits such as reduced multiplicity which means fewer individual detector elements are needed, enhanced rate capabilities, and reduced thickness of the entire detector [25]. Nevertheless, this design has not been adopted for the DHCAL prototype since it requires gluing the electronics, which would create a tight gas gap.

### 5.1.2 Readout Electronics and Cassette Structure

A 180 $fC$ threshold is set for each readout cell to detect the passage of particles through the gas gap, without measuring the deposited energy. The overall energy of a particle shower is estimated by counting the total number of hits in an event, where a ”hit” is recorded whenever a particle traverses a cell. Each RPC consists of two $32 \times 48$ $cm^2$ readout boards, each with 1536 $1 \times 1$ $cm^2$ pads on the anode side of the chamber. With three RPCs per layer, this configuration results in a total of 9216 readout channels per layer. To define hits, the Digital Calorimetry (DCAL) chip version III readout system applies a single threshold to the output signal of an $8 \times 8$ readout pads [26, 27]. The data acquisition system collects signals from the RPCs and transmits them to a computer, synchronized by a 10 $MHz$ clock, yielding a 100 $ns$ time resolution.

The DHCAL records data from each hit in the following format: $t$ $x$ $y$ $z$ , where $t$ denotes the timestamp of the hit signal, $x$ and $y$ correspond to the coordinates of the hit pad, each ranging from 0 to 95 cm, and $z$ represents the number of the layer in which the hit occurred.

## 5.2 DHCAL with Minimal Absorber

The Min-DHCAL that was used to take data in November 2011 did not include any absorber layers between the cassettes serving as the active layers, resulting in the expansion of the showers on a much greater volume, which in turn produces finer granularity and better spatial resolution. The Min-DHCAL comprised 50 cassettes, with a spacing of 2.54 cm between them. The thickness of each cassette was approximately 12.5 mm, equivalent to about 0.3 radiation lengths ($X_0$) or 0.034 nuclear interaction lengths ($\lambda_I$), corresponding to an overall thickness of the stack of about 15 $X_0$ or 1.7 $\lambda_I$. The Min-DHCAL consisted of a total of 460800 readout channels, representing a world record in calorimetry for High Energy Physics at the time. Figure 5.2 displays a photograph of the Min-DHCAL. In this thesis, lower energy levels in the 1-10 GeV range are analyzed, where the showers fill the detector's volume, allowing for a detailed capture of their characteristics.

## 5.3 Fermilab Test Beam Setup

The Fermilab Test Beam Facility (FTBF) [18], providing a primary proton beam with an energy of 120 GeV and secondary beams with energies ranging from 1 to 66 GeV composed of electrons, muons, and pions, was used to collect data through the Min-DHCAL.

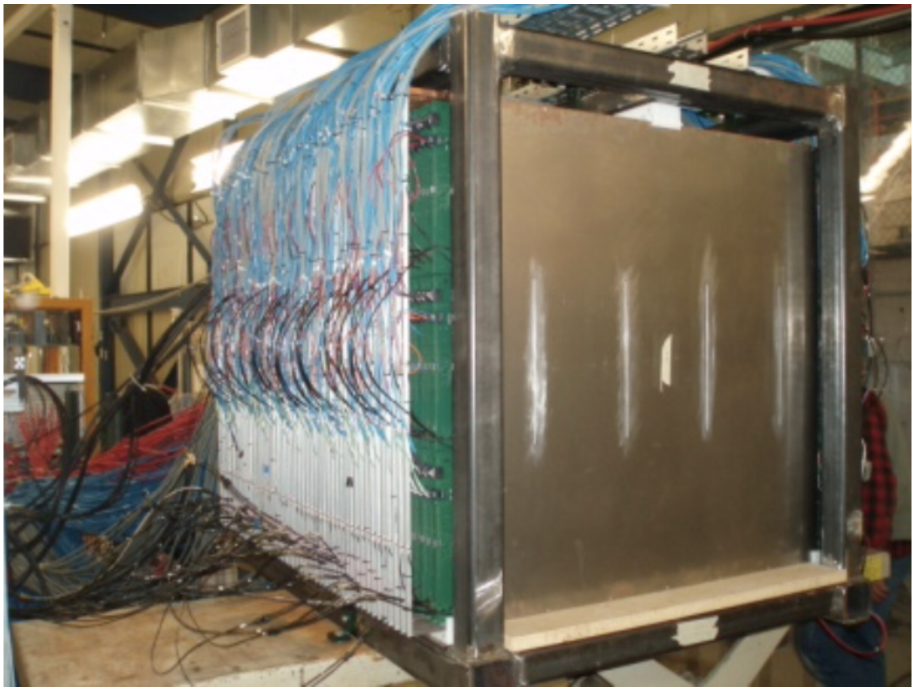

**Figure 5.2:** The Min-DHCAL at Fermilab in November 2011 [28].

Particles were delivered every minute in spills lasting 4 seconds, where the electrons were the predominant component at energies below 6 GeV, and pions were the predominant component at higher energies. As shown in Figure 5.3, two Cherenkov counters were used for particle identification, and two 19 $\times$ 19 $cm^2$ scintillator paddles were positioned approximately two meters upstream of the Min-DHCAL. The signal from the Cherenkov counters was incorporated into the data stream and used offline to distinguish positrons from muons and pions. The simulations accounted for the Cherenkov counters and trigger counters in the upstream material from the beam to the detector.

Since one of the Cherenkov counters, serving as the muon tagger was not working, only one Cherenkov counter has been used in the data collected in November 2011. The three gas mixtures used in RPCs are blended on-site and subsequently delivered to a gas distribution system comprising 28 individually controlled channels. Figure 5.4 shows the test beam setup at the FTBF.

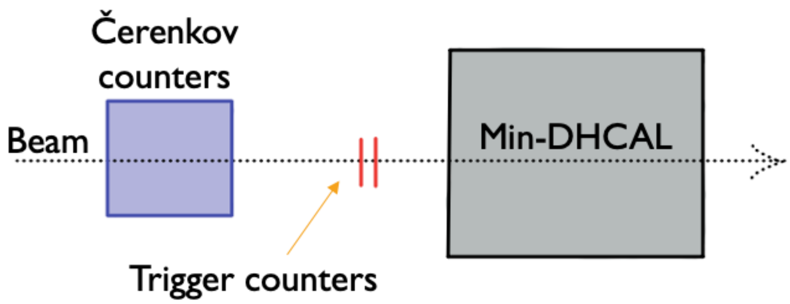


**Figure 5.3:** The sketch of the test beam setup at Fermilab, including the scintillator trigger and the Cherenkov counters.

**Figure 5.4:** Photograph of the test beam setup at FTBF [29]

# Chapter 6

# Analysis

The results of the analysis using test beam data collected with the DHCAL with Minimal absorber (Min-DHCAL) at Fermilab will be discussed below.

## 6.1 Collected Data

This study is based on the data collected in November 2011. A total of 804,433 events were collected within an energy range of 1-10 GeV. Table 6.1 illustrates the distribution of events across the different energy values for the good runs. The data files include hits generated by particles interacting with the detector. Therefore, a "good" test run was defined as one devoid of layers either recording an unusually high number of hits or failing to record any hits at all. This happened in a small fraction ($< 10\%$) of the time and was mostly related with some intermittent issues in the readout electronics.

| Energy [GeV] | Runs | Number of Events |
|---|---|---|
| 1 | 3 | 107386 |
| 2 | 2 | 107213 |
| 3 | 5 | 61919 |
| 4 | 2 | 83565 |
| 6 | 1 | 109486 |
| 8 | 3 | 108862 |
| 10 | 7 | 226002 |
| **Total** | **23** | **804433** |

**Table 6.1:** Number of events for each beam energy for the November 2011 data set.

The Application Specific Integrated Circuits (ASIC) developed to read out the test beam prototype consist of $8 \times 8$ pad configuration. Less than 1 % of the ASICs in the Min-DHCAL were non-functional and did not record any hits. Although no correction was applied to the data, these dead ASICs were accounted for in the Monte Carlo simulations by removing all hits produced in the corresponding dead areas. Since most hits are recorded in the center of a layer, only dead ASICs located in the center of a layer significantly impact the data. For 6, 8, and 10 GeV energies, only one layer featured a dead ASIC in such a critical location.

## 6.2 Run parameters

Figure 6.1 provides an example of the Standard Plots for a 6 GeV Min-DHCAL run. The Standard Plots represent the primary features of a test run by displaying significant characteristics of the events derived from the data. They include 1D histograms and 2D scatter plots, showcasing combinations of the key run parameters.

1. The distribution of the total number of hits recorded in the Min-DHCAL for an event facilitates particle identification by effectively differentiating the muons from pions or positrons.

2-4. X, Y, and Z hit distributions.

5-7. XZ, XY, YZ 2D projection of the hit distributions.

8-10. The ratio of hits recorded in the first five, ten, and fifteen layers to the total number of hits in an event is used as a tool to separate electromagnetic and hadronic showers.

11-13. 2D projection of the ratio of hits as a function of hits.

14. After performing particle identification, the maximum layer reached by particles in an event can be used to confirm the expected characteristics of pion showers.

15. Maximum dispersion is useful for distinguishing between muons and showers, helping to analyze the spread of particle showers.

16. Depth indicates the final layer a particle reaches from the test beam before initiating a shower, used in particle identification by comparing positron and pion showers

17. The length of the particle shower provides a measure of the longitudinal extent of the shower's development.

18. To visualize the lateral dispersion of hits within a single event, the RMS value of the event in the XY plane of the detector is used.

19-22. 2D projections of the plots.

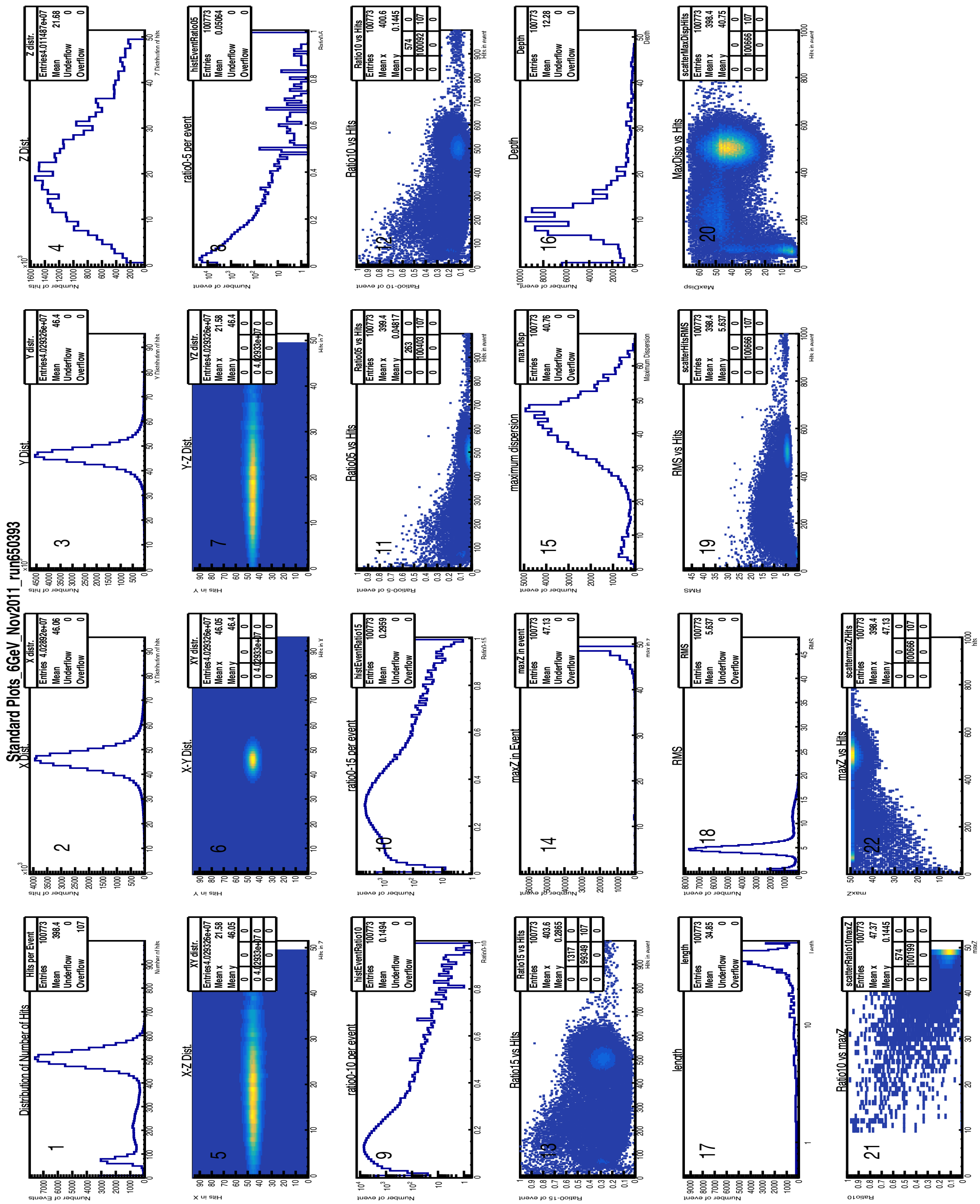

**Figure 6.1:** Standard Plots for a 6 GeV test run for Min-DHCAL in November 2011.

## 6.3 Event Selection

In order to eliminate the noise hits and double hits, which are produced by multiple interactions of particles with the same cell, and particles that start showering before entering the detector, the following event selection criteria are applied.

The fraction of events that survive the selection cuts is summarized in Table 6.2, which combines the percentage of events that meet the various event selection criteria for both data and pion simulation.

| **Energy [GeV]** | **Cut** | **1** | **2** | **3** | **4** | **6** | **8** | **10** |
|---|---|---|---|---|---|---|---|---|
| **Data** | Timing Cuts | 99.99 | 99.99 | 99.98 | 99.97 | 99.99 | 99.99 | 99.99 |
| | More than 5 Active Layers | 96.39 | 98.29 | 99.42 | 97.85 | 99.93 | 99.83 | 99.90 |
| | First Layer Cluster requirement | 67.42 | 64.22 | 57.13 | 55.21 | 71.60 | 68.38 | 70.35 |
| **Simulation** | Timing Cuts | 100 | 100 | 100 | 100 | 100 | 100 | 100 |
| | More than 5 Active Layers | 98.02 | 99.70 | 99.93 | 99.96 | 99.99 | 99.99 | 99.99 |
| | First Layer Cluster requirement | 82.35 | 80.44 | 79.32 | 79.2 | 80.17 | 79.81 | 79.73 |

**Table 6.2:** Percentage of events surviving the event selection cuts for data and simulation.

### 6.3.1 Timing cuts

The trigger is processed after the hits are recorded. Hits are recorded across seven consecutive time-bins, each with a duration of 100 $ns$, and have time differences ranging from 15 to 21 time-bins relative to the trigger timestamp; therefore, hits with larger time differences correspond to those occurring earlier in the event. Most hits from a shower are recorded within the same time-bin, as the passage of a relativistic particle through the detector is approximately 3 $ns$, which is much shorter than the 100 $ns$ timing resolution. Particles that are responsible for triggering the event are mostly captured in just two of the seven time bins: 19 and 20. It is assumed that hits in time-bin 15 to 18 are from particles exiting the detector, and hits in time-bin 21 are from particles that entered the detector before the trigger.

In a small fraction of events, the majority of hits are recorded outside time-bins 19 and 20. Using the timing information, these events are rejected, and the fraction of multiple-particle events is reduced.

### 6.3.2 More than 5 active layers

A small fraction (less than a few percents) of events were actually empty, either because of data acquisition handshaking issues at the beginning of runs, or sometimes triggered by intermittent noise. To eliminate these, events with less than 5 layers with recorded hits are excluded, which would remove approximately 1-4% of the events in the data and less than 2% in the simulation.

### 6.3.3 Requirements on the first layer

As described in section 4.4, a nearest neighbor algorithm is used to cluster the hits in the first layer of an event. Each event must contain precisely one cluster with no more than four hits in the first layer. This event selection cut excludes events with multiple particles, and those where the particles begin showering before entering the detector, which would result in either a large number of hits or multiple identified clusters in the first layer.

## 6.4 Particle Identification

As the Fermilab test beam comprises a mixture of muons, positrons, and pions, Particle IDentification (PID) must be applied. Figure 6.2 shows the effectiveness of the particle identification cuts applied on the hit distribution. PID was performed offline using the Cherenkov counter and the concept of an interaction layer. A Cherenkov signal indicates positrons, while pions and muons are required to show no Cherenkov signal.

Additionally, pions are identified by the presence of an interaction layer, which marks the start of an electromagnetic or hadronic shower. In this analysis, an interaction layer is defined as the first layer in a sequence of at least five consecutive layers, each with four or more hits. The pion data sample will suffer from low statistics at low energies, particularly since the beam is dominated by positrons below 6 GeV. Muons are identified by requiring tracks to pass through at least 35 layers with at least one hit each, without the presence of an interaction layer.

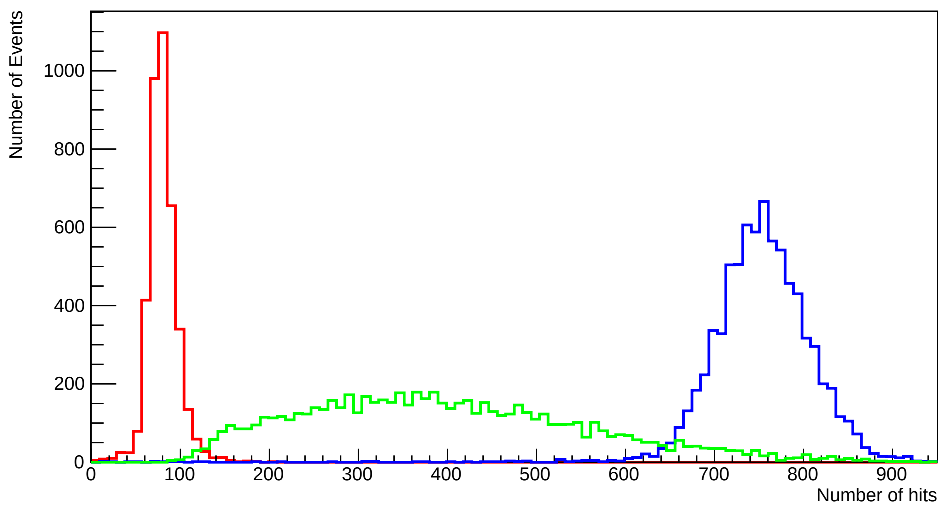


**Figure 6.2:** Hit distribution for a 10 GeV run. The selected muons are shown in red, pions in green, and positrons in blue

Aligning with the theoretical expectations, as seen from Figure 6.2, muons generate the fewest hits, forming a narrow distribution; pions exhibit a broader distribution due to their interaction via both electromagnetic and hadronic processes, additionally, since the Min-DHCAL does not have an absorber to contain the full size of the showers, particularly the hadronic ones, a lower number of hits than expected is recorded due to leakage; and positrons, interacting solely through electromagnetic processes, produce dense electromagnetic showers in the detector, resulting in a high number of hits and a narrow distribution.

Table 6.3 presents the number of particles surviving the particle identification cuts, both for data and simulation.

| **Energy [GeV]** | **Particles** | **1** | **2** | **3** | **4** | **6** | **8** | **10** |
|---|---|---|---|---|---|---|---|---|
| **Data** | Positrons | 70123 | 69581 | 30779 | 21559 | 59450 | 46701 | 70286 |
| | Pions | 644 | 1179 | 2229 | 5013 | 14014 | 21663 | 61924 |
| | Muons | 5047 | 2358 | 9845 | 27158 | 9196 | 12301 | 30510 |
| **Pion Simulation** | Pions | 400 | 3020 | 6120 | 8860 | 10620 | 10580 | 10780 |

**Table 6.3:** Number of events selected as positrons, pions, and muons for data and pion simulation.

Figure 6.3 presents event displays for a typical 10 GeV pion, muon, and positron. The 3D distribution, along with the XY, ZY, and XZ projections of the hits in Min-DHCAL are shown, respectively.

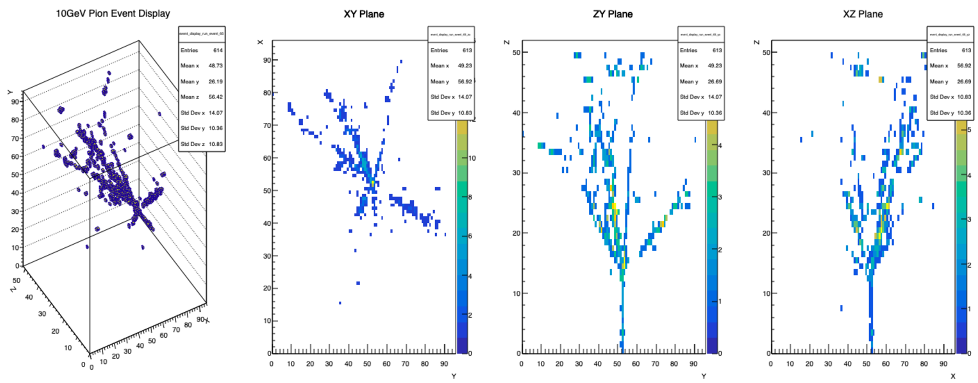


**(a)** Pion event

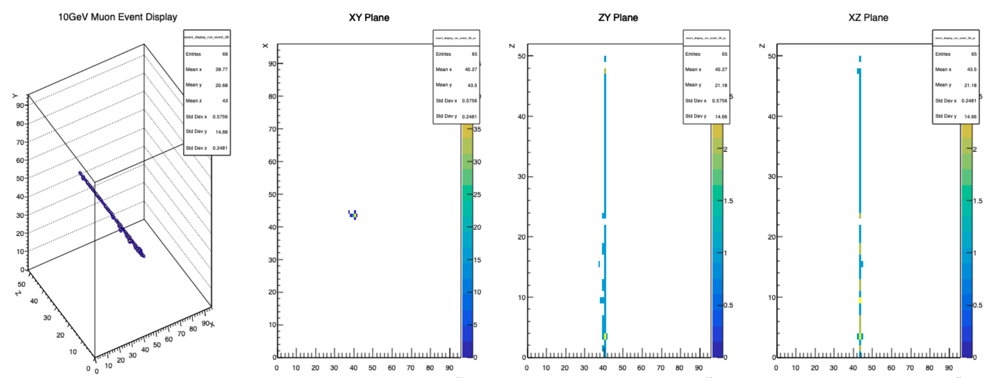


**(b)** Muon event

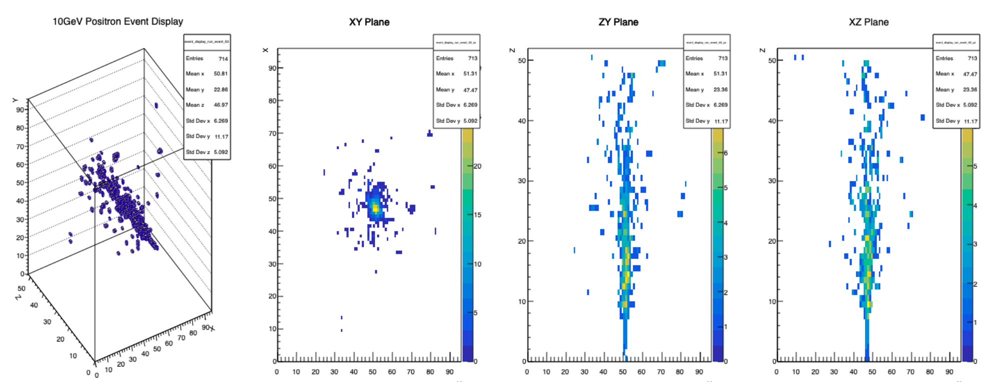


**(c)** Positron event

**Figure 6.3:** Example of 3D and 2D event displays for a November 2011 test run at 10 GeV: (a) shows a typical pion shower, (b) shows a typical through-going muon, and (c) shows a typical positron shower, captured in the Min-DHCAL.

## 6.5 Calibration of the Min-DHCAL

The noise rate, minimum ionizing particles detection efficiency, pad multiplicity, and the performance of RPCs were measured to be dependent on environmental parameters, such as pressure and temperature. Adjustments were made to account for the discrepancies in the performance characteristics of each RPC, to enhance the uniformity of RPC response across different runs. The average correction factors display minimal variation with energy, allowing for a unified calibration procedure to be applied across all energy levels [30, 31].

### 6.5.1 Equalisation

The ratio of tracks that result in at least one recorded hit compared to the total number of identified tracks, is defined as the efficiency $\epsilon$. The pad multiplicity $\mu$, represents the mean number of hits recorded for tracks that produce at least one hit within the chamber. By utilizing the efficiency $\epsilon_i$ and average pad multiplicity $\mu_i$ for each $RPC_i$ and the average RPC efficiency $\epsilon_0$, and pad multiplicity of the entire stack, 0.96 and 1.56 respectively [32], the calibration factor $C_i$ per data taking run is calculated as:

$$C_i = \frac{\epsilon_i \mu_i}{\epsilon_0 \mu_0} \tag{6.1}$$

After determining the calibration factors $C_i$ for each $RPC_i$, the corrected number of hits $N'$ is calculated as the sum of the hits $N_i$ recorded in each $RPC_i$, multiplied by its respective calibration factor $C_i$.

$$N' = \sum_{i=0} N_i \cdot C_i \tag{6.2}$$

### 6.5.2 Equalisation test

The distribution of all calibration factors from November 2011, is shown in Figure 6.4 to assess the normalization of the calibration. While the distribution is not perfectly Gaussian, the central part of the distribution is fitted with a Gaussian function.

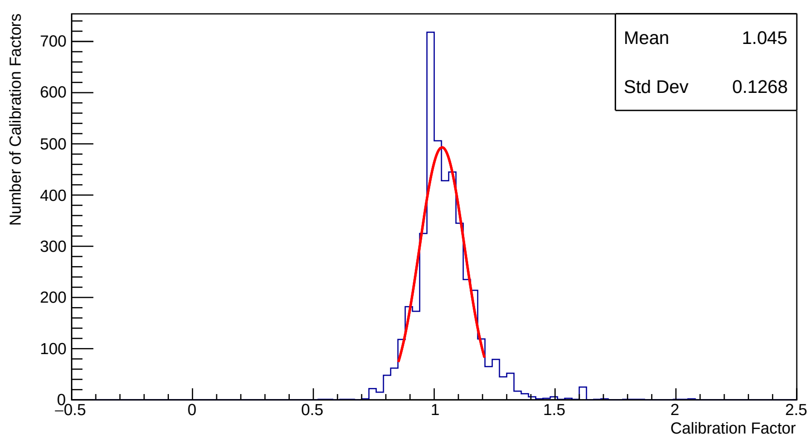


**Figure 6.4:** Distribution of the calibration factor for all runs

The calibration does not significantly alter the mean response, as the mean of the Gaussian function is close to one and the width is $\sigma = 0.128$.

The primary goal of the equalization is to enhance the pion resolution and to achieve a uniform response for all runs at each energy point compared to an uncalibrated result.

Figure 6.5 shows the hit distribution of 6 GeV pion events both calibrated (blue) and uncalibrated (red).

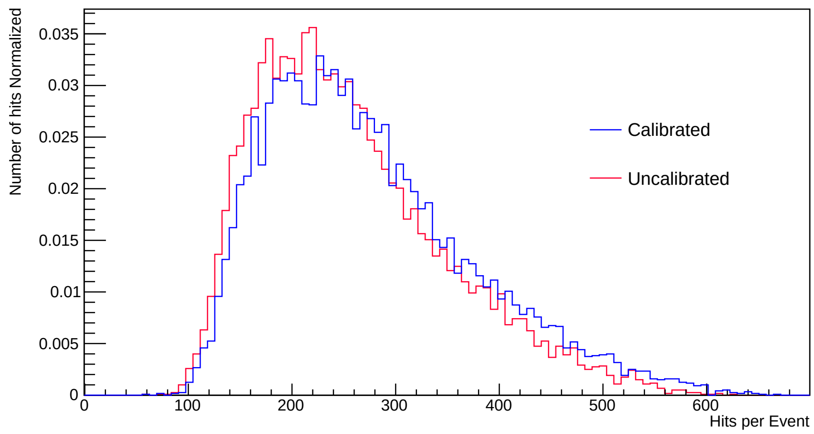


**Figure 6.5:** Hit distribution of 6 GeV pion, calibrated data shown in blue and uncalibrated data in red.

The calibration must ensure that the mean of the hit distribution for different particles remains unaffected by varying operating conditions. Figure 6.6, shows the mean position of 10 GeV pion, both before and after calibration equalization. The calibrated means exhibit significantly less scatter compared to the uncalibrated data. However, there is a notable 4% increase in the mean response.

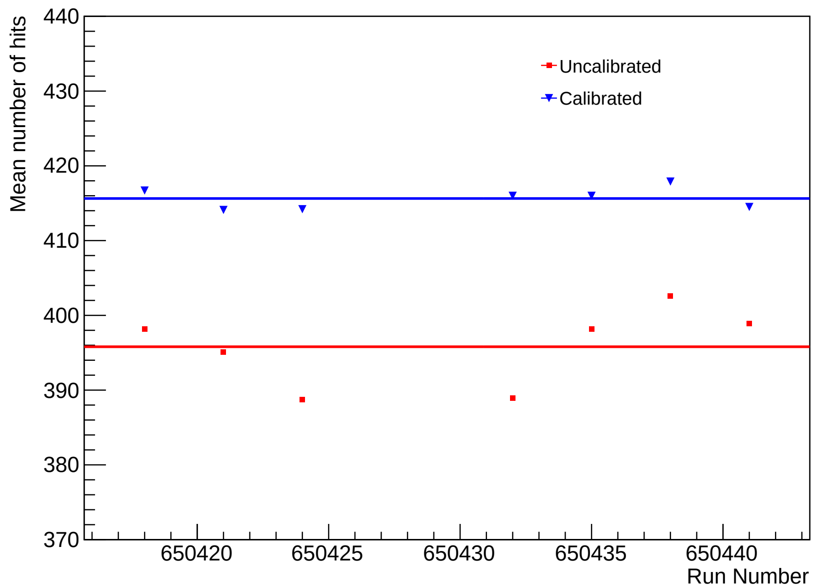


**Figure 6.6:** Average number of hits of 10 GeV pions for different runs before (red) and after (blue) calibration, fitted with a constant solid line. The uncertainties in the average number of hits, derived from the hit distribution plots (Figure 7.1), are not shown in this plot. Uncertainties will be discussed in Section 7.5.

## 6.6 Monte Carlo Simulation

The Min-DHCAL test beam setup is modelled with the GEANT4 software package [33, 34]. The GEANT4 software toolkit employs multiple models to simulate the interactions of particles with matter. Simulation of hadronic showers is considerably challenging as they are notably complex and involve a large number of physical processes. The variation in hit multiplicity and efficiency per RPC are averaged across the entire prototype and modelled by the digitizer of the RPC response called RPCSIM [35].

### 6.6.1 Digitisation of the RPC response

To identify the pads with hits, the RPCSIM program generates a signal charge Q for each point, distributes this charge across the pads, sums the charges on each pad, and applies a threshold $T$. The signal charges are generated based on the measured spectrum of avalanche charges from cosmic rays. The amount of the deposited energy is disregarded when generating a signal since the avalanche size is minimally influenced by the deposited energy. However, it highly depends on the initial ionization location within the gas gap [36, 37].

The measured spectrum of avalanche charges, $N(Q)$, used to generate the signal charges, is fitted to the following functional form:

$$N(Q) = \alpha Q^{\beta} e^{-\gamma Q}, \tag{6.3}$$

where $\alpha$, $\beta$, and $\gamma$ are parameters that depend on the operating high voltage. $Q$ represents the charge. If another avalanche is already forming nearby, the electric field will be reduced, therefore, the chance of an electron gaining enough energy to start a Townsend avalanche decreases in an RPC's gas gap. A scaling factor $s$ is applied to energy deposits that are close in both space and time, to simulate this effect. GEANT4 provides the timing information for these deposits. The distances $d_{dist}$ between all energy deposits in the same layer are calculated to find the impacted energy deposits. If two deposits are within a certain distance $d_{cut}$, the charge of the later deposit is scaled by $s$, which ranges from 0 to 1 and increases linearly with $d_{dist}$. The diagram in Figure 6.7 shows how the scaling factor $s$ changes with the distance $d_{dist}$.

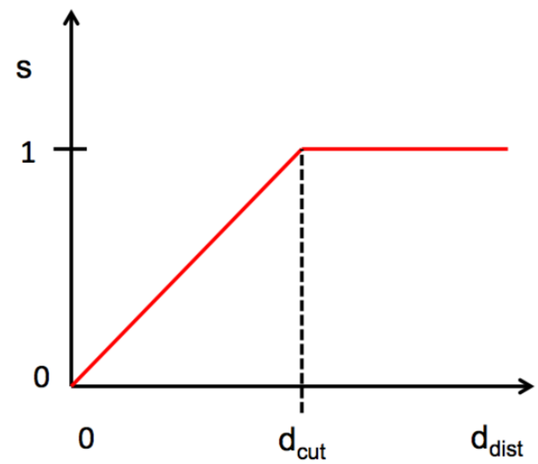


**Figure 6.7:** Diagram showing how the scaling factor $s$ depends on the distance $d_{dist}$ between GEANT4 energy depositions [37]

Further to account for possible discrepancies between charge distribution measured in the laboratory and those obtained in the test beam setup, an additional parameter $Q_0$ is introduced. The modified charge is given by Equation 6.4:

$$Q' = Q + Q_0 \tag{6.4}$$

Subsequently, the generated charge is dispersed across the anode plane as a function of the lateral distance $r$ from the ionization point. This dispersion utilizes the ratio $R$ of the means of two Gaussian distributions to balance their contributions, along with the standard deviations $\sigma_1$ and $\sigma_2$ of these distributions, as shown in Equation 6.5.

$$f(r) = (1 - R)e^{(-\frac{r^2}{2\sigma_1^2})} + Re^{(-\frac{r^2}{2\sigma_2^2})} \tag{6.5}$$

Once the charges from all avalanches are allocated to the readout pads, the total charge on each pad is calculated and a threshold $T$ is applied.

### 6.6.2 Physics lists

Limitations of perturbative quantum chromodynamics (pQCD) at low energies present significant challenges for the simulation of hadronic showers. Moreover, accurately modeling experimental effects like non-compensation, and leakage, and describing jets, isolated electrons, and photons adds further complexity [38]. Since no single theory accurately describes hadron interactions across all energies and particle species, GEANT4, by covering a wide range of hadronic interaction energies, provides a general modelling framework that is categorized into physics lists. These lists, each with specific upper and lower energy thresholds of validity, allow different implementations of processes and models. The highly segmented CALICE prototypes are ideal for validating these models with experimental data. The key features of the string parton models, cascade models, precompound models, and electromagnetic models [39, 40] are outlined below:

- *String Parton Models*: GEANT4 offers two distinct methods to simulate the interactions of medium or high-energy hadrons with nuclei: the Fritiof (FTF) model and the Quark Gluon String (QGS) model. In the FTF model, the diffractive scattering of the primary particle with nucleons occurs solely through momentum exchange. Conversely, the QGS model mediates the hadron-nucleon interaction via pomerons. The interaction between the primary particle and the nucleus results in one or more excited strings and an excited nucleus. The fragmentation of these excited strings into hadrons is managed by the longitudinal string fragmentation model, with specific variations between the FTF and QGS models.

- *Cascade Models*: For medium and low energy interactions, where the quark structure of individual nuclei can be disregarded, the Bertini cascade (BERT) model is used [41]. The BERT model represents a nucleus as a sphere with uniform nucleon density. Secondary particles are produced when incident hadrons strike protons and neutrons in the target nucleus. Subsequently, these secondary particles interact with other nucleons, creating an intra-nuclear cascade. Following this cascade, the excited nucleus is modelled as a collection of particle-hole states, which then undergo decay through pre-equilibrium, nuclear explosion, fission, and evaporation processes.

- *Precompound Models*: The interaction of secondary particles with the excited nucleus is managed either by a shower model or by a precompound model, that involves string parton models labelled with a "P" suffix (FTFP and QGSP). The precompound model is used to simulate the final state of hadron inelastic scattering. It describes the emission of protons, neutrons, and light ions that occurs before the nuclear system achieves equilibrium. The resulting products are then transferred to de-excitation models.

- *Electromagnetic Models*: Includes models for simulation of electromagnetic processes such as ionization, Bremsstrahlung, pair production, and photon interactions. EMZ is the most precise option available in the EM model.

In this analysis, the following simulations using different physics lists were produced to be compared to the data: FTFP-BERT, FTFP-BERT-EMZ, QGSP-BERT, and QGSP-BERT-EMZ. These simulations are produced with 400 $\mu m$ $d_{cut}$ and a 250 fC threshold.

# Chapter 7

# Results

This thesis analyzes test beam data collected with the Min-DHCAL at Fermilab in November 2011. A general description of the calorimeter's response to pions is provided, followed by an in-depth analysis and hit density distributions. The results of this analysis are compared with GEANT4-based simulations, testing the simulation itself and different physics lists against the pion data.

## 7.1 Response to Pions

Pions behave much like a Minimum Ionizing Particle (MIP), creating narrow, minimum ionizing tracks with only a few hits per layer, until they interact hadronically, causing an extensive hadronic shower.

### 7.1.1 Hit Distributions

Figure 7.1 and Figure 7.2 illustrate the pion response at energies from 1 to 10 GeV, where the hit distributions are broad at higher energies due to significant fluctuations in deposited energy from hadronic interactions and leakage.

Figure 7.1 includes simulations using FTFP-BERT-EMZ with 0.64 (blue), 0.32 (black), and 0.48 (green) $X_0$ upstream material. Figure 7.2 includes simulations using FTFP-BERT (blue), QGSP-BERT (black), and QGSP-BERT-EMZ (green) models all with 0.64 $X_0$ upstream material. FTFP-BERT with 0.64 $X_0$ upstream material can serve as a reference for further development and tuning of the simulations. Both the data and simulation distributions are normalized to unity. Simulations from different physics lists agree with each other in terms of both peak and shape, and they all match the data in the overall shape of the distributions. However, there is a noticeable shift in the peak of the simulated distributions for all energies except 4 GeV. This suggests that further tuning or development of the simulation parameters is necessary. However, the simulations agree well with positron data analysis; see [1].

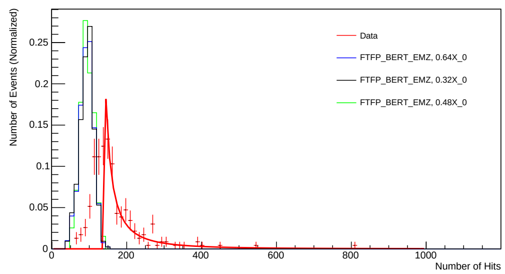


**(a)** Hit distribution of 1 GeV pions

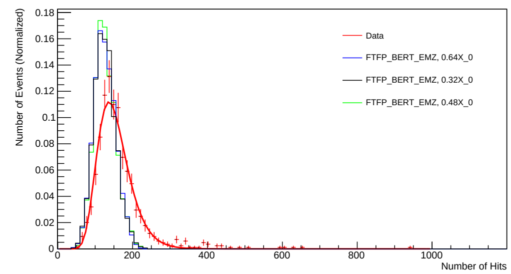


**(b)** Hit distribution of 2 GeV pions

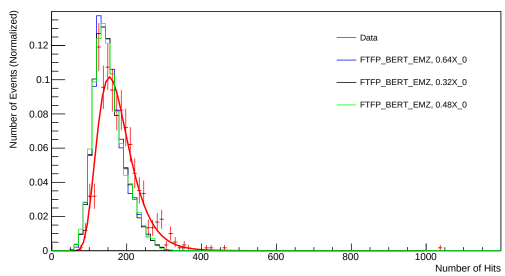


**(c)** Hit distribution of 3 GeV pions

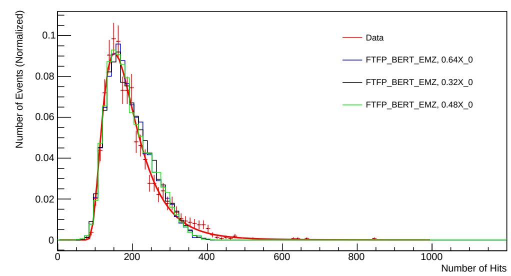


**(d)** Hit distribution of 4 GeV pions

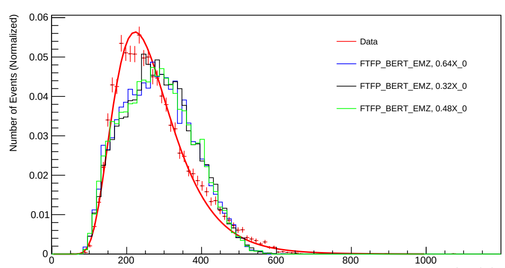


**(e)** Hit distribution of 6 GeV pions

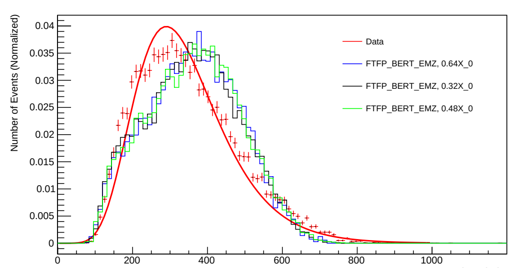


**(f)** Hit distribution of 8 GeV pions

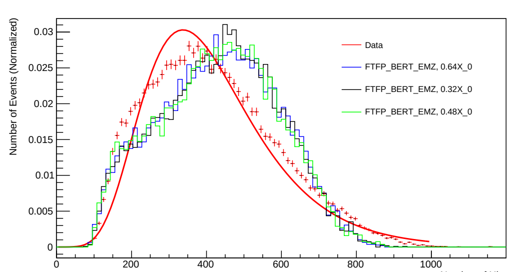


**(g)** Hit distribution of 10 GeV pions

**Figure 7.1:** Hit distribution for data and simulations for ranges of pion energies. Simulations were generated using FTFP-BERT-EMZ with 0.64 (blue), 0.32 (black), and 0.48 (green) $X_0$ upstream material. The data is fitted with the Novosibirsk function shown as a solid line.

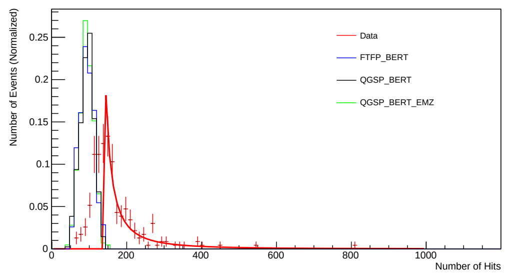


**(a)** Hit distribution of 1 GeV pions

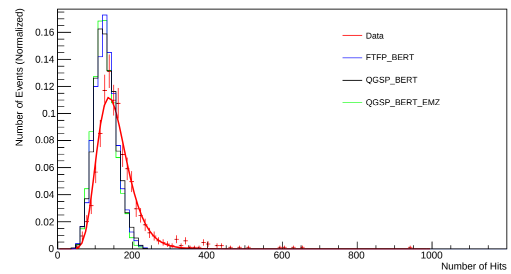


**(b)** Hit distribution of 2 GeV pions

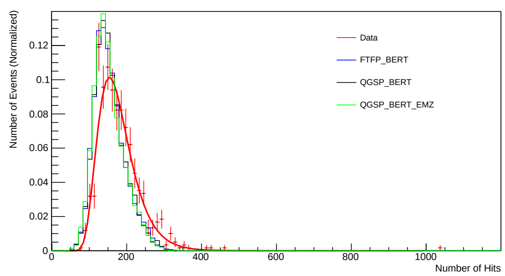


**(c)** Hit distribution of 3 GeV pions

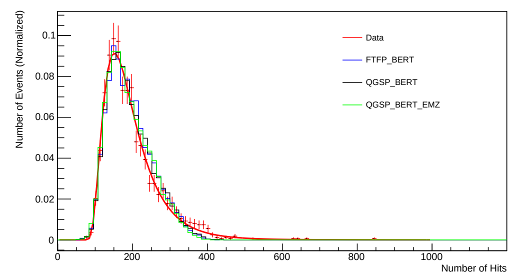


**(d)** Hit distribution of 4 GeV pions

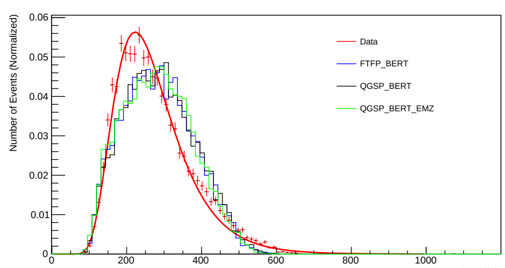


**(e)** Hit distribution of 6 GeV pions

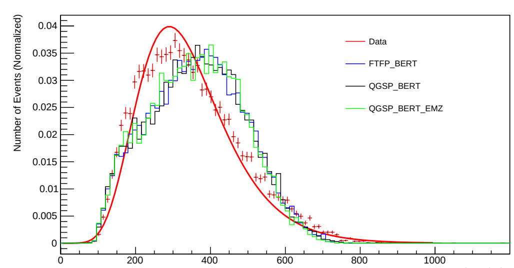


**(f)** Hit distribution of 8 GeV pions

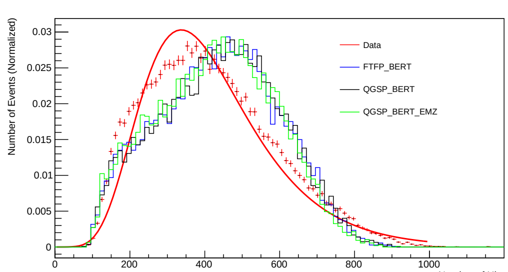


**(g)** Hit distribution of 10 GeV pions

**Figure 7.2:** Hit distribution for data and simulations for ranges of pion energies. Simulations were generated using FTFP-BERT (blue), QGSP-BERT (black), and QGSP-BERT-EMZ (green) models with 0.64 $X_0$ upstream material. The data is fitted with the Novosibirsk function shown as a solid line.

The asymmetric responses do not fit a Gaussian distribution. Therefore, both responses are fitted using a Novosibirsk function [42] within a $3\sigma$ of the peak's range. The Novosibirsk function is defined as follows:

$$F(x) \equiv Ne^{(-\frac{1}{2\sigma_0^2}ln^2(1-\frac{x-x_0}{\sigma_E}\eta)-\frac{\sigma_0^2}{2})}, \tag{7.1}$$

where:

- $x_0$: the peak value

- $\eta$: the asymmetry parameter

- $N$ the normalization factor

- $\sigma_0 = (\frac{1}{\sqrt{ln4}}sinh^{-1}(\eta\sqrt{ln4}))$

- $\sigma_E$: the resolution

This function fits the responses well, particularly at low energies of 2, 3, and 4 GeV, but not at 1 GeV, where there are hardly any pions.

### 7.1.2 Linearity of the Response

The mean response as a function of the beam energy for both data and simulation is shown in Figure 7.3 and Figure 7.4. Both data and the simulations are fitted in the range of 3-10 GeV with a power law shown as a solid line of the form:

$$N_{hit} = aE_{beam}^m \tag{7.2}$$

The exponent $m$ in this power law quantifies the non-linearity, or saturation, of the response. A value of $m = 1$ signifies a linear response, while $m < 1$ indicates saturation. Due to the digital readout and limited granularity, only one hit is recorded in a cell, whereas within a core of particle showers, multiple particles can traverse a single cell. This results in response saturation. The fit accurately represents the data, with an exponent of $m = 0.75$ suggesting significant saturation and possibly also leakage. Table 7.1, summarizes the fit parameters of the power law fit for both the data and the simulated pion response in the range of 3-10 GeV.

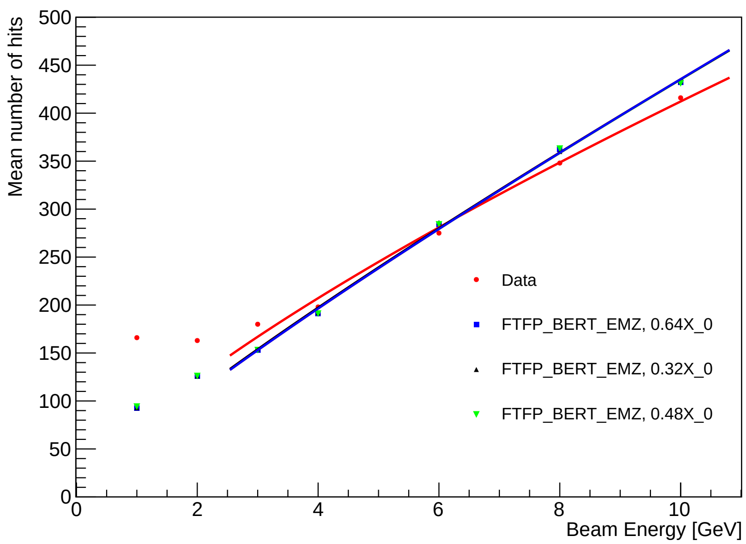


**Figure 7.3:** Mean response of pions as a function of beam energy is presented for both data (red) and simulations. Different physics lists are shown as FTFP-BERT-EMZ with 0.64 (blue), 0.32 (black), and 0.48 (green) $X_0$ upstream material. Both data and simulation are fitted in a range of 3-10 GeV with a power law shown in a solid line.

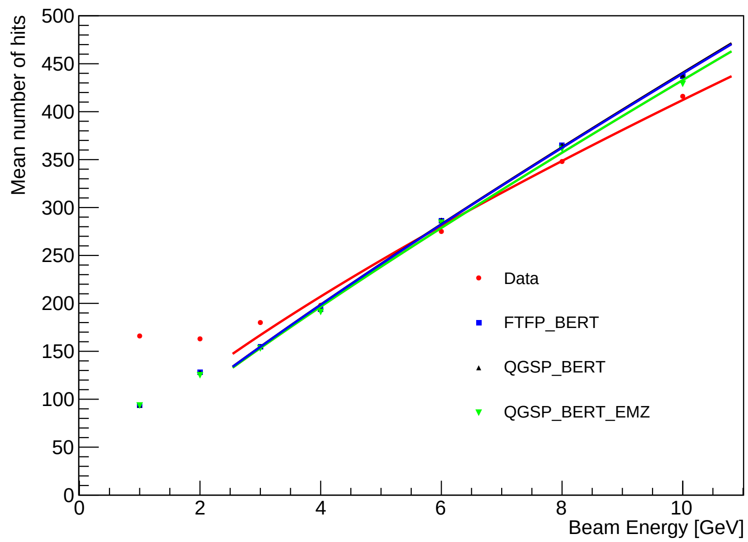


**Figure 7.4:** Mean response of pions as a function of beam energy is presented for both data (red) and simulations. Different physics lists are shown as FTFP-BERT (blue), QGSP-BERT (black), and QGSP-BERT-EMZ (green) with 0.64 $X_0$ upstream material. Both data and simulation are fitted in a range of 3-10 GeV with a power law shown in a solid line.

| | $a$ | $m$ |
|---|---|---|
| Data | $0.751 \pm 0.04$ | $73.2 \pm 6.2$ |
| FTFP-BERT-EMZ with 0.64 $X_0$ | $0.869 \pm 0.021$ | $58.84 \pm 2.5$ |
| FTFP-BERT-EMZ with 0.32 $X_0$ | $0.864 \pm 0.02$ | $59.6 \pm 2.2$ |
| FTFP-BERT-EMZ with 0.48 $X_0$ | $0.867 \pm 0.023$ | $59.04 \pm 2.7$ |
| FTFP-BERT | $0.868 \pm 0.017$ | $59.6 \pm 2.07$ |
| QGSP-BERT | $0.869 \pm 0.017$ | $59.56 \pm 2.1$ |
| QGSP-BERT-EMZ | $0.862 \pm 0.023$ | $59.48 \pm 2.8$ |

**Table 7.1:** Fit parameters of the power law fit for the pion data and the simulations.

### 7.1.3 Calibration Response

Using the method described in section 6.5, the data and simulation responses follow the same pattern and show good agreement at 6 GeV. However, they deviate at lower and higher energies, with the simulations exhibiting an upward shift at higher energies, and the data at lower energies. At lower energies, the beam contains only a small fraction of pions. Consequently, even minor contamination by muons and positrons can dominate the response, causing a shift in the observed data.

The calibrated pion energy distributions at energies from 1 to 10 GeV are shown in Figure 7.5 and Figure 7.6. The data distributions are fitted with a Novosibirsk function plotted as a solid line. Both the data and simulation distributions are normalized to unity. The calibrated distributions are broad, reflecting the characteristics of hadronic interactions. Similar to the hit distributions, simulations from different physics lists agree with each other in terms of both peak and shape, and they all match the data in the overall shape of the distributions. However, there is a noticeable shift in the peak of the simulated distributions for all energies except 4 GeV. At higher energies, the data distributions show a large tail, which is not present in the simulations and may be a test of the simulation of the leakage. A general good agreement is observed between the calibrated constructed energy distributions and the hit distributions for all energies.

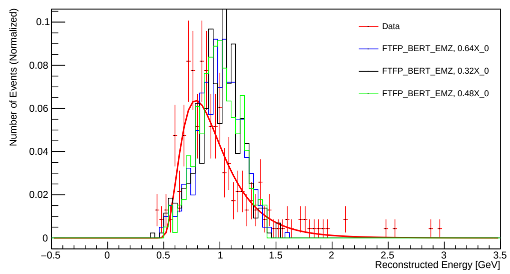


**(a)** Energy reconstruction of 1 GeV pions

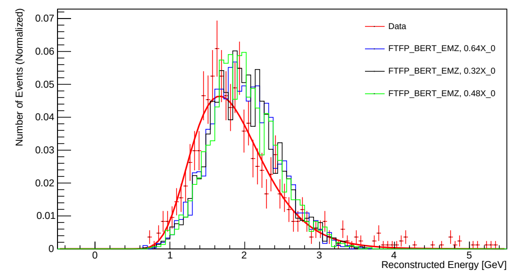


**(b)** Energy reconstruction of 2 GeV pions

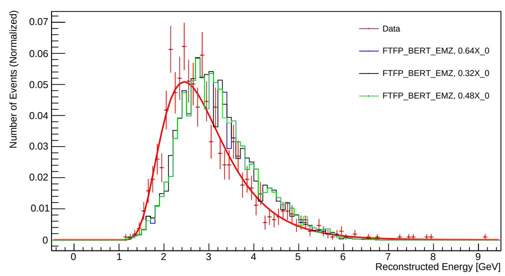


**(c)** Energy reconstruction of 3 GeV pions

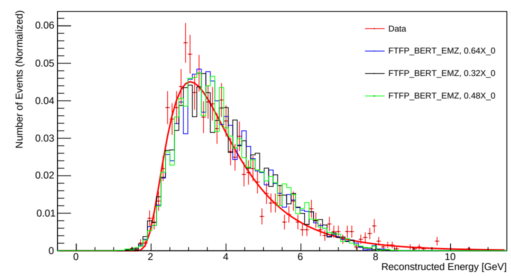


**(d)** Energy reconstruction of 4 GeV pions

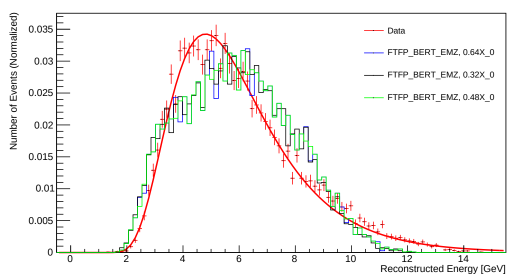


**(e)** Energy reconstruction of 6 GeV pions

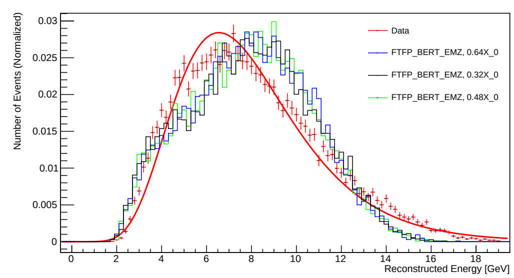


**(f)** Energy reconstruction of 8 GeV pions

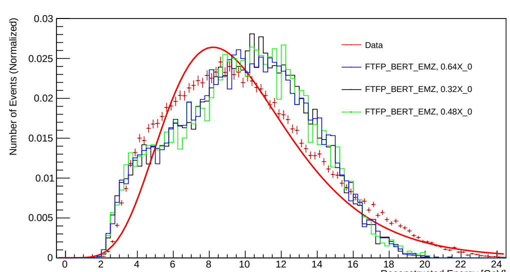


**(g)** Energy reconstruction of 10 GeV pions

**Figure 7.5:** Energy Reconstruction for data and simulations for ranges of pion energies. Simulations were generated using FTFP-BERT-EMZ with 0.64 (blue), 0.32 (black), and 0.48 (green) $X_0$ upstream material.

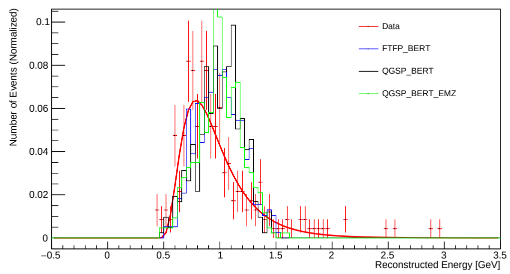


**(a)** Energy reconstruction of 1 GeV pions

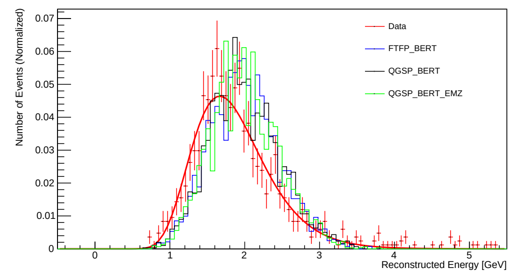


**(b)** Energy reconstruction of 2 GeV pions

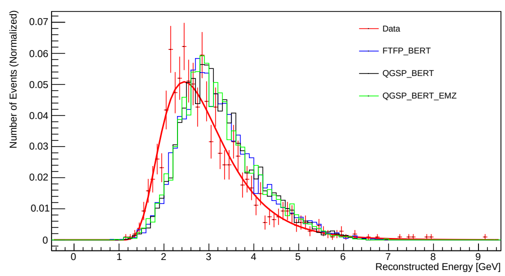


**(c)** Energy reconstruction of 3 GeV pions

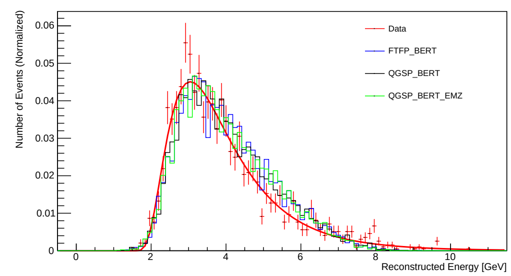


**(d)** Energy reconstruction of 4 GeV pions

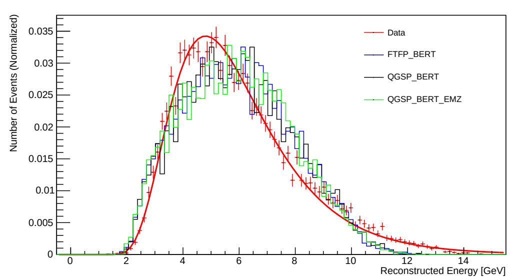


**(e)** Energy reconstruction of 6 GeV pions

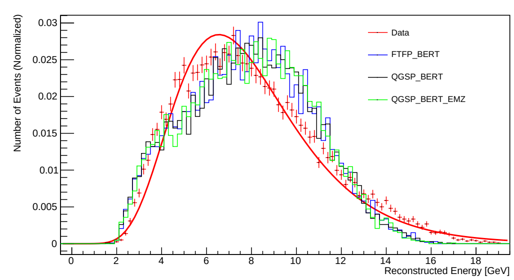


**(f)** Energy reconstruction of 8 GeV pions

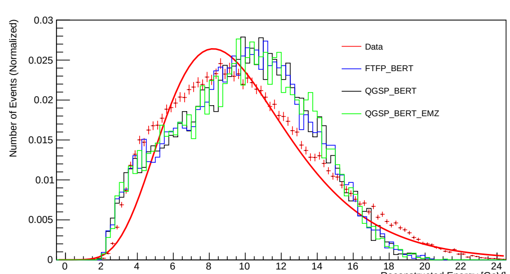


**(g)** Energy reconstruction of 10 GeV pions

**Figure 7.6:** Energy Reconstruction for data and simulations for ranges of pion energies. Different physics lists are shown as FTFP-BERT (blue), QGSP-BERT (black), and QGSP-BERT-EMZ (green) with 0.64 $X_0$ upstream material.

### 7.1.4 Energy Resolution

To measure the precision of energy measurements of pions, the energy resolution is evaluated. By using the width ($\sigma$) and the most probable value ($E_{mean}$) obtained from the fit of the reconstructed energy distributions, the resolution is calculated as the ratio $\sigma/E_{mean}$. The energy resolution as a function of beam energy for both the experimental and the two sets of simulations is shown in Figure 7.7 and Figure 7.8.

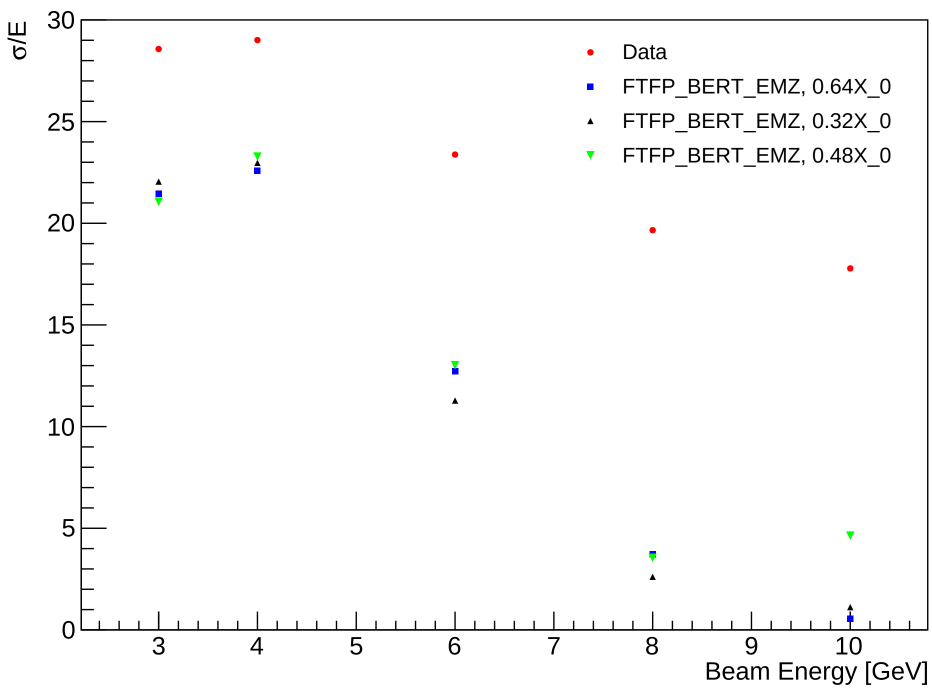


**Figure 7.7:** The energy resolution of pions as a function of beam energy is presented for both data (red) and simulations. Different physics lists are shown as FTFP-BERT-EMZ with 0.64 (blue), 0.32 (black), and 0.48 (green) $X_0$ upstream material. The uncertainties on the data points are too small to be visible at the scale of the plot and will be discussed in Section 7.5.

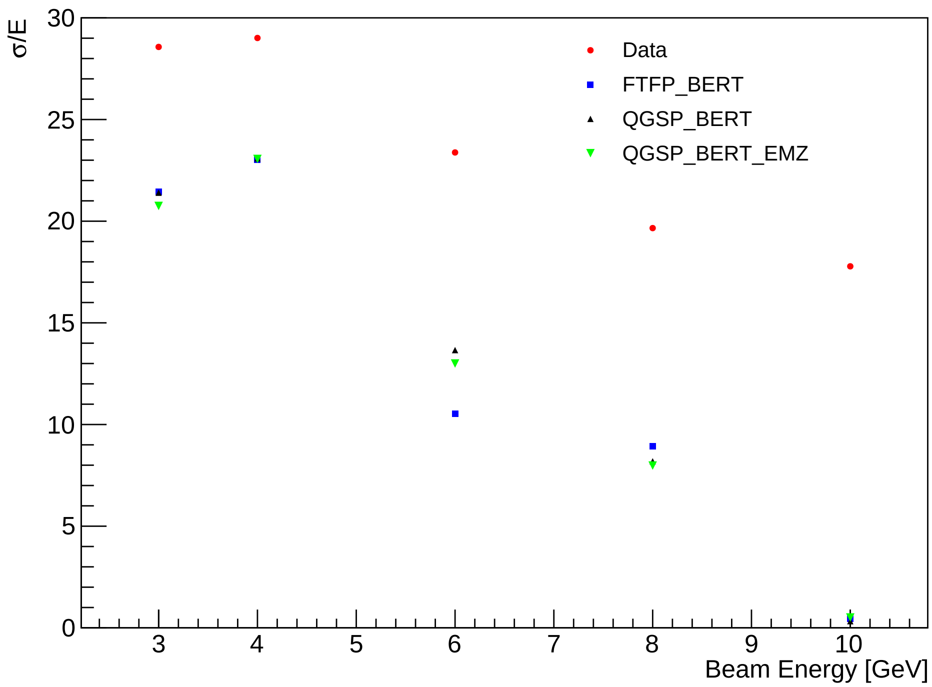


**Figure 7.8:** The energy resolution of pions as a function of beam energy is presented for both data (red) and simulations. Different physics lists are shown as FTFP-BERT (blue), QGSP-BERT (black), and QGSP-BERT-EMZ (green) with 0.64 $X_0$ upstream material. The uncertainties on the data points are too small to be visible at the scale of the plot and will be discussed in Section 7.5.

The resolution is degraded by the significant energy loss due to the leakage of pion showers. While it is possible to correct for this leakage on average, the extent of leakage is subject to considerable fluctuations. These fluctuations compromise the resolution, requiring event-by-event correction, which is highly challenging. Simulations yield a better energy resolution than that observed in the data, suggesting potential leakage in the data and limitations in the simulations. The resolution for 1 and 2 GeV pions, which were also excluded from the power law fit, is not displayed in the resolution results.

## 7.2 Longitudinal Shower Profile

The high number of readout channels of the Min-DHCAL provides an exceptional tool for in-depth analysis of shower shapes. For instance, the longitudinal shower profile of 4 GeV pion events is shown in Figure 7.9, fitted with a gamma distribution fit [43] as shown in Equation 7.3.

$$f(l) = E_0 \frac{(\frac{l-\mu}{\beta})^{\gamma-1} e^{-\frac{t-\mu}{\beta}}}{\beta\Gamma} \tag{7.3}$$

$E_0$ represents the energy of the incident particle, $\Gamma$ denotes the Gamma function, $\gamma$ is a shape parameter, $\mu$ is a location parameter related to the depth at which the shower initiates, shifting the distribution in $l$, and $\beta$ is a normalization parameter. Using the fit parameter, the shower maximum can be determined as shown in Equation 7.4.

$$l_{max} = \gamma\beta - \beta + \mu \tag{7.4}$$

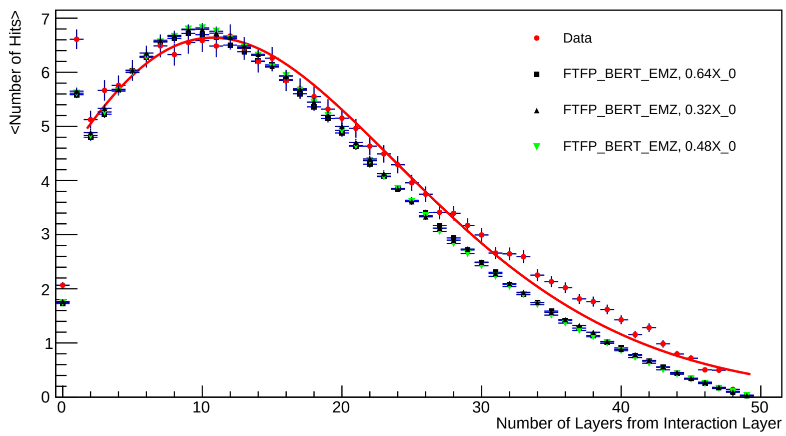


**Figure 7.9:** Distribution of the longitudinal distribution for 4 GeV pion. Different physics lists FTFP-BERT (blue), QGSP-BERT (black), and QGSP-BERT-EMZ (green) are shown. Data is fitted to a gamma distribution function plotted as a solid line.

The shower maximum, determined through fitting, is summarized for both data and simulation in Table 7.2.

| Energy [GeV] | 3 | 4 | 6 | 8 | 10 |
|---|---|---|---|---|---|
| Data shower maximum [layer] | $10.81 \pm 0.1$ | $10.74 \pm 0.1$ | $13.3 \pm 0.1$ | $11.16 \pm 0.1$ | $16.03 \pm 0.1$ |
| Simulation shower maximum [layer] | $8.88 \pm 0.1$ | $11.03 \pm 0.1$ | $13.03 \pm 0.1$ | $10.6 \pm 0.1$ | $15.42 \pm 0.1$ |

**Table 7.2:** Fit parameters for the pion data and the simulations.

The described fit accurately represents both the data and the simulation. The simulation shows hits in the final layers, with the data indicating more hits in the later layers. Except for 4 and 6 GeV, where the shower maximum position aligns for both data and simulation, the data shows the shower maximum occurring approximately 1-2 layers later than in the simulation.

Due to event-to-event variability in the interaction layer's position, the longitudinal shower profile is analyzed by plotting the average number of hits against the layer numbers from the interaction layer. Before the interaction layer, pions behave as minimum ionizing particles (MIPs), with a gradually increasing response, consistent with simulations. The response shows approximately 2 hits per layer near the interaction layer, followed by a sharp increase in the average number of hits starting from the interaction layer. The longitudinal shower profile for a range of 3 to 10 GeV pion events is shown in Figure 7.10 and Figure 7.11.

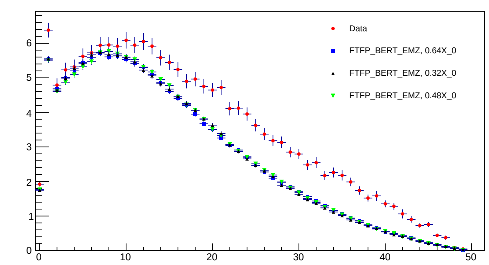


**(a)** Longitudinal shower of 3 GeV pions

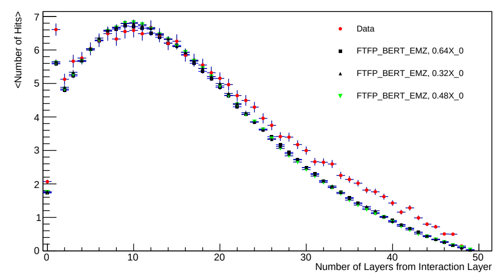


**(b)** Longitudinal shower of 4 GeV pions

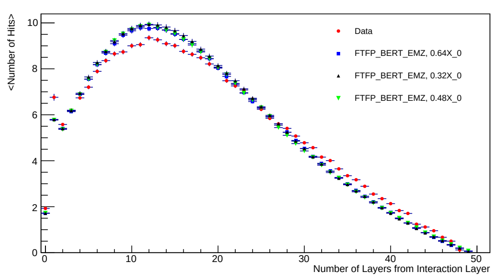


**(c)** Longitudinal shower of 6 GeV pions

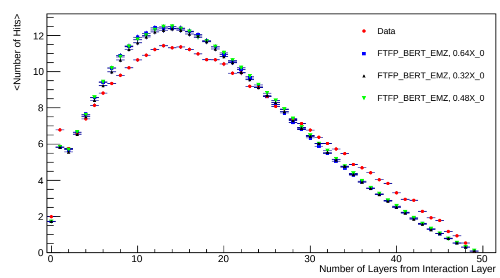


**(d)** Longitudinal shower of 8 GeV pions

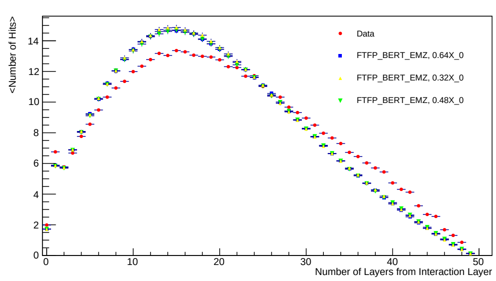


**(e)** Longitudinal shower of 10 GeV pions

**Figure 7.10:** Longitudinal pion shower distribution for data (red) and simulation using different physics lists: FTFP-BERT-EMZ with 0.64 (blue), 0.32 (black), and 0.48 (green) $X_0$ upstream material.

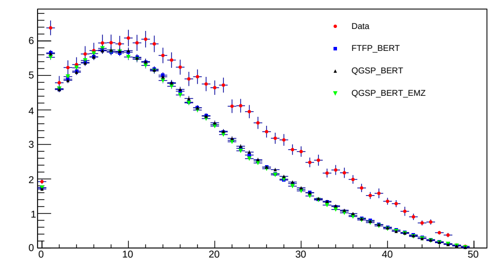


**(a)** Longitudinal shower of 3 GeV pions

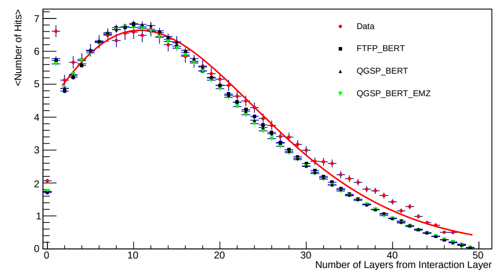


**(b)** Longitudinal shower of 4 GeV pions

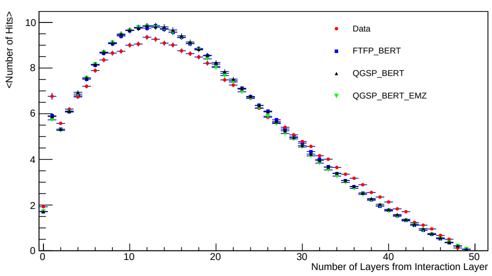


**(c)** Longitudinal shower of 6 GeV pions

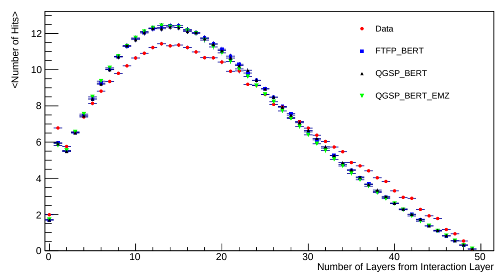


**(d)** Longitudinal shower of 8 GeV pions

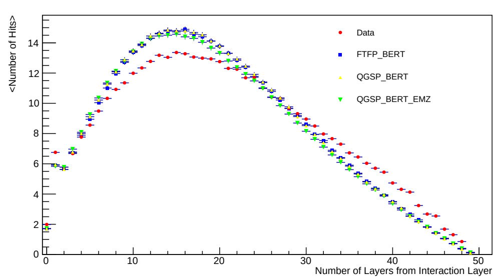


**(e)** Longitudinal shower of 10 GeV pions

**Figure 7.11:** Longitudinal pion shower distribution for data (red) and simulation using different physics lists: FTFP-BERT (blue), QGSP-BERT (black), and QGSP-BERT-EMZ (green) with 0.64 $X_0$ upstream material.

Longitudinal shower profile of pion events initiating their showers across different layer ranges for all energy levels has been analyzed. Figure 7.12 presents the longitudinal profile for 6 GeV pion events. The last layers are incomplete due to the detector's construction. The overall shape of the distribution shows a good agreement between data and simulation for all events, regardless of the starting layer. However, events that start their showers at later layers, exhibit more distinct differences. Specifically, for events beginning their showers in later layers, there are more hits observed in the simulations compared to the data.

Mean longitudinal dispersion (see section 6.2) is another critical parameter for comparison. The longitudinal dispersion for each event is calculated as follows:

$$D_z = \sqrt{\frac{\sum z_i^2}{N} - (\frac{\sum z_i}{N})^2} \tag{7.5}$$

The sum is over all hits $i$ in an event, $z_i$ is the layer of each hit, and $N$ is the total number of hits. Figure 7.13 and Figure 7.14 show the mean longitudinal dispersion as a function of beam energy. Except for 1 GeV pions, a good agreement between data and simulation is observed.

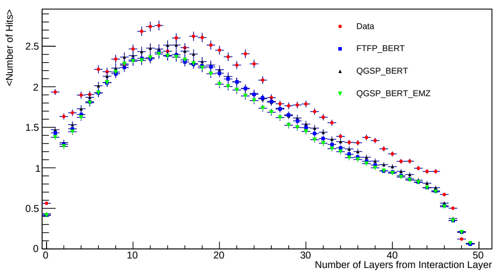


**(a)** Shower starting between layers 0 to 4

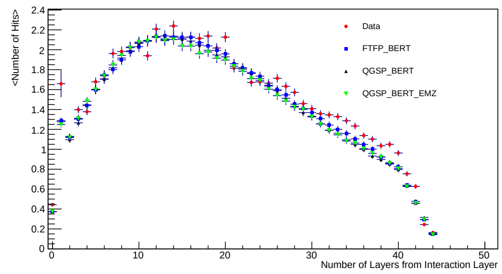


**(b)** Shower starting between layers 5 to 9

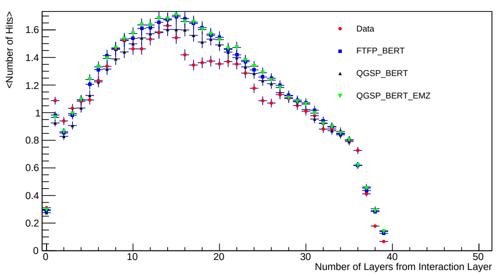


**(c)** Shower starting between layers 10 to 14

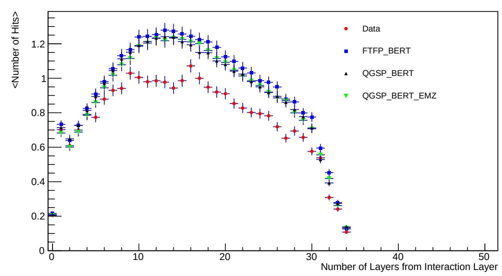


**(d)** Shower starting between layers 15 to 19

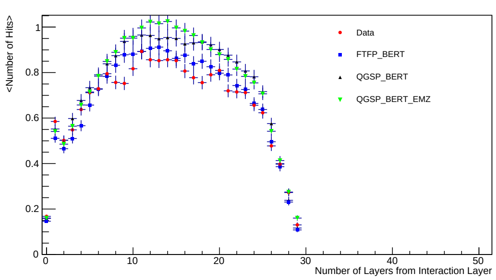


**(e)** Shower starting between layers 20 to 24

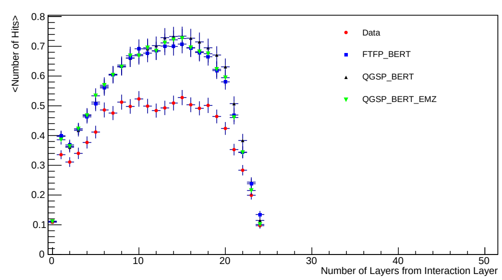


**(f)** Shower starting between layers 25 to 29

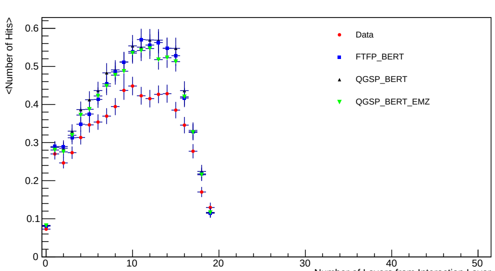


**(g)** Shower starting between layers 30 to 34

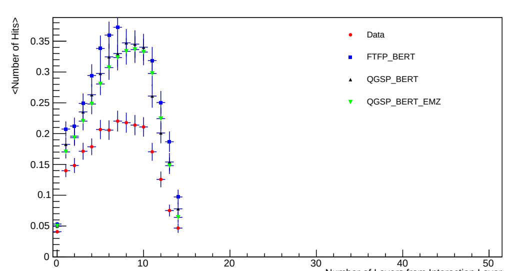


**(h)** Shower starting between layers 35 to 39

**Figure 7.12:** Longitudinal distribution for 6 GeV pion events starting their showers across different layer ranges. Data (red) and simulation using different physics lists: FTFP-BERT (blue), QGSP-BERT (black), and QGSP-BERT-EMZ (green) with 0.64 $X_0$ upstream material are shown.

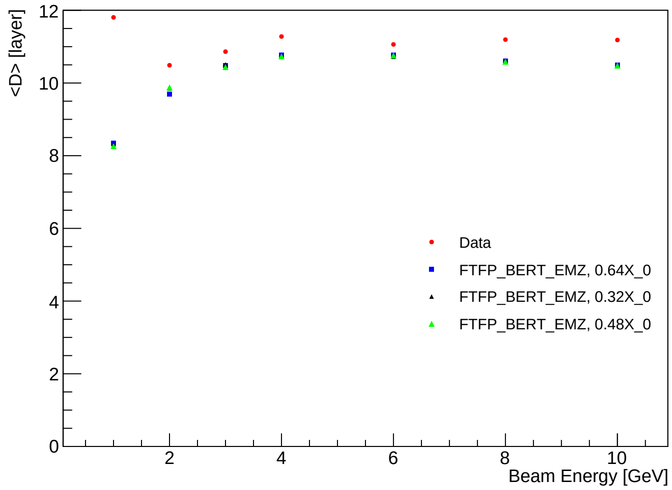


**Figure 7.13:** Mean longitudinal dispersion of hits for pions. Different physics lists FTFP-BERT-EMZ with 0.64 (blue), 0.32 (black), and 0.48 (green) $X_0$ upstream material are shown. Data is plotted in red.

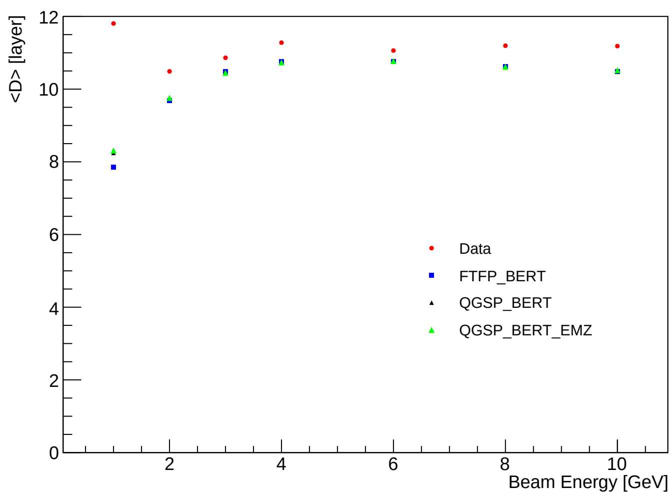


**Figure 7.14:** Mean longitudinal dispersion of hits for pions. Different physics lists FTFP-BERT (blue), QGSP-BERT (black), and QGSP-BERT-EMZ (green) are shown. Data is plotted in red.

## 7.3 Transverse Shower Profile

To measure the transverse shower shape, the shower's central axis is identified. Each event undergoes separate linear fitting to the hits in both XZ and YZ planes to identify the shower's central axis. Subsequently, the radius $R$ is calculated as the perpendicular distance from this axis. Figure 7.15 and Figure 7.16 present the radial shower profile of 3 to 10 GeV pions, comparing the data with the simulations.

The transverse shower shape shows good agreement between the data and simulation across all radii. Both data and simulation locate the maximum of the RMS distribution at around 4-7 cm. The areas in both plots are normalized to one event. At 3 GeV, all physics lists show good agreement with the data. However, no model fully matches the data at other energies.

Figure 7.17 and Figure 7.18 illustrate the mean distance, calculated by averaging over all events and hits at a given energy, to compare the transverse showers of data and simulation across the entire energy range. At 6 GeV, there is a good agreement between the data and the simulation. However, at lower energies, the average radial distance is greater in the simulations, while at higher energies, it is greater in the data.

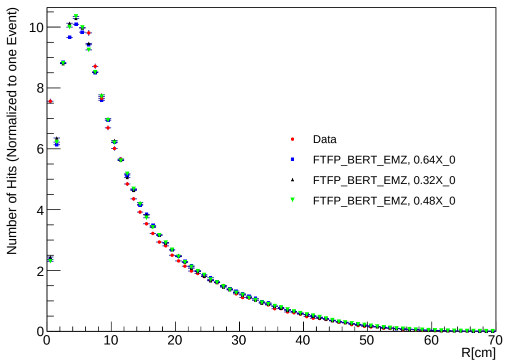


**(a)** Radial shower distributions of 3 GeV pions

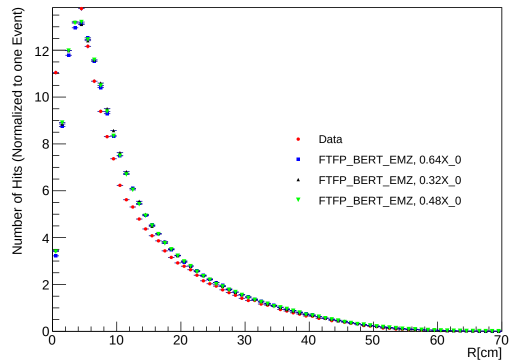


**(b)** Radial shower distributions of 4 GeV pions

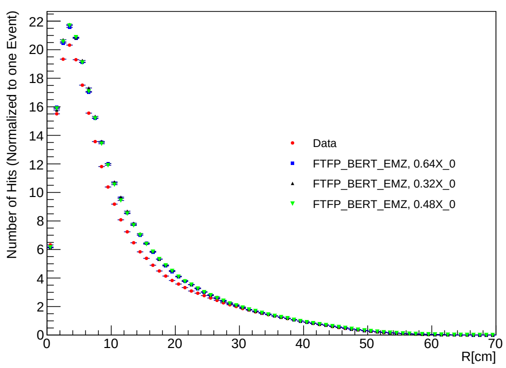


**(c)** Radial shower distributions of 6 GeV pions

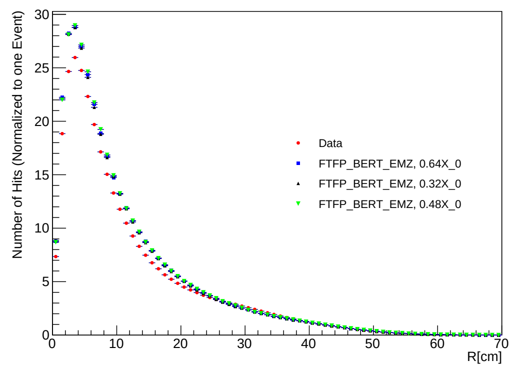


**(d)** Radial shower distributions of 8 GeV pions

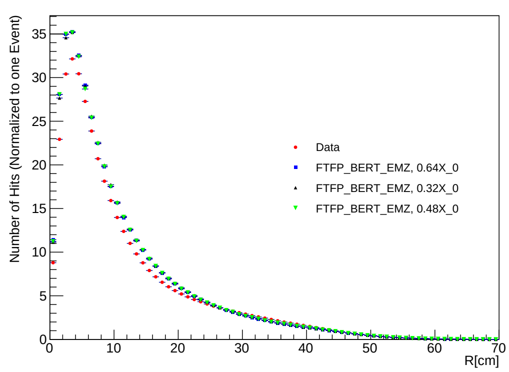


**(e)** Radial shower of 10 GeV pions

**Figure 7.15:** Radial distribution for pion data (red) and simulation using different physics lists: FTFP-BERT-EMZ with 0.64 (blue), 0.32 (black), and 0.48 (green) $X_0$ upstream material.

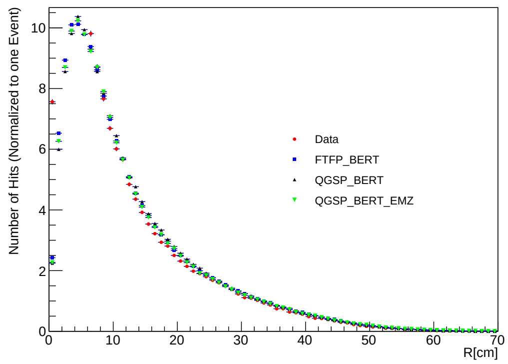


**(a)** Radial shower distributions of 3 GeV pions

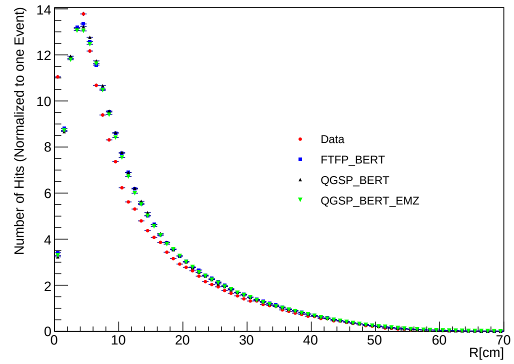


**(b)** Radial shower distributions of 4 GeV pions

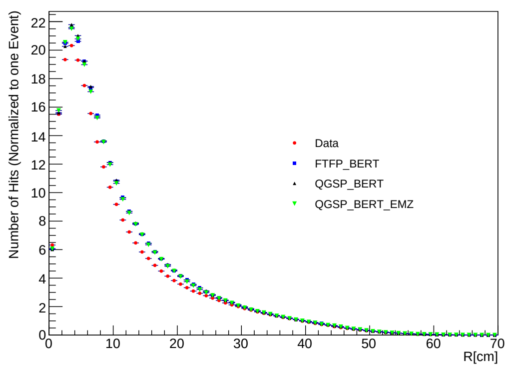


**(c)** Radial shower distributions of 6 GeV pions

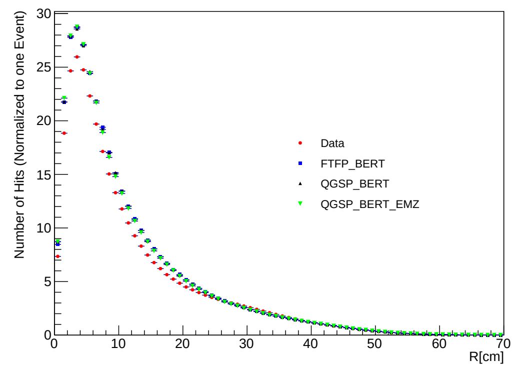


**(d)** Radial shower distributions of 8 GeV pions

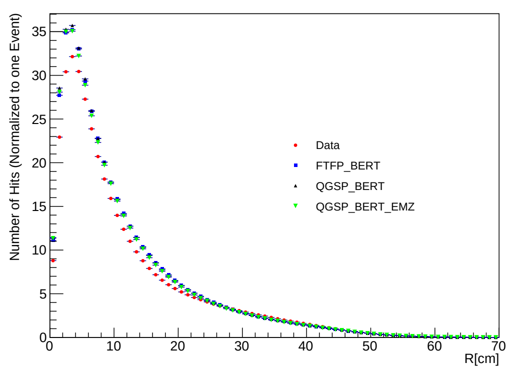


**(e)** Radial shower distributions of 10 GeV pions

**Figure 7.16:** Radial distribution for pion data (red) and simulation using different physics lists: FTFP-BERT (blue), QGSP-BERT (black), and QGSP-BERT-EMZ (green) with 0.64 $X_0$ upstream material.

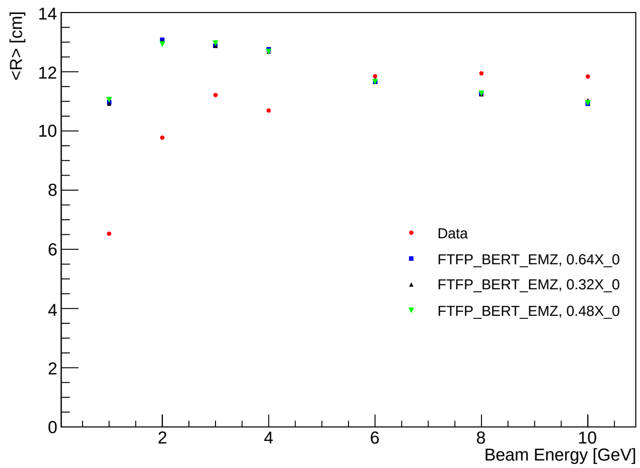


**Figure 7.17:** Mean radial distance of hits in a pion event. Different physics lists FTFP-BERT-EMZ with 0.64 (blue), 0.32 (black), and 0.48 (green) $X_0$ upstream material are shown. Data is plotted in red.

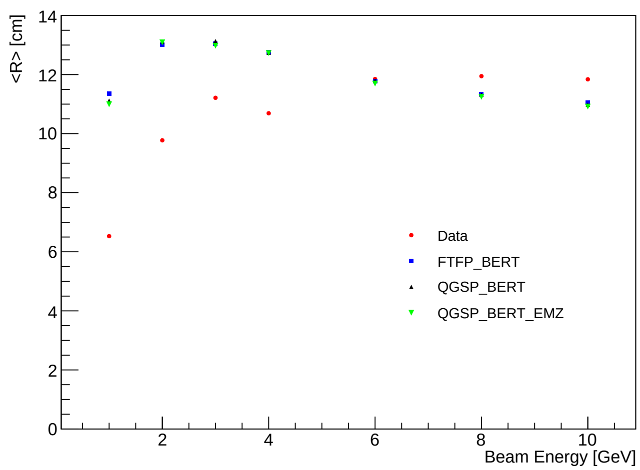


**Figure 7.18:** Mean radial distance of hits in a pion event. Different physics lists FTFP-BERT (blue), QGSP-BERT (black), and QGSP-BERT-EMZ (green) with 0.64 $X_0$ upstream material are shown. Data is plotted in red.

The radial dispersion of hits in an event is calculated similarly to longitudinal dispersion, using Equation 7.6:

$$D_R = \sqrt{\frac{\sum R_i^2}{N} - (\frac{\sum R_i}{N})^2} \tag{7.6}$$

Where $R_i$ is the radius of each hit, and $N$ is the total number of hits in an event. Figure 7.19 and Figure 7.20 display the average radial dispersion as a function of beam energy. As expected from the average radius, the dispersion of pion shower is larger in the simulations, while at higher energies, it is greater in the data, indicating the simulation underestimates the size of the showers for higher energies.

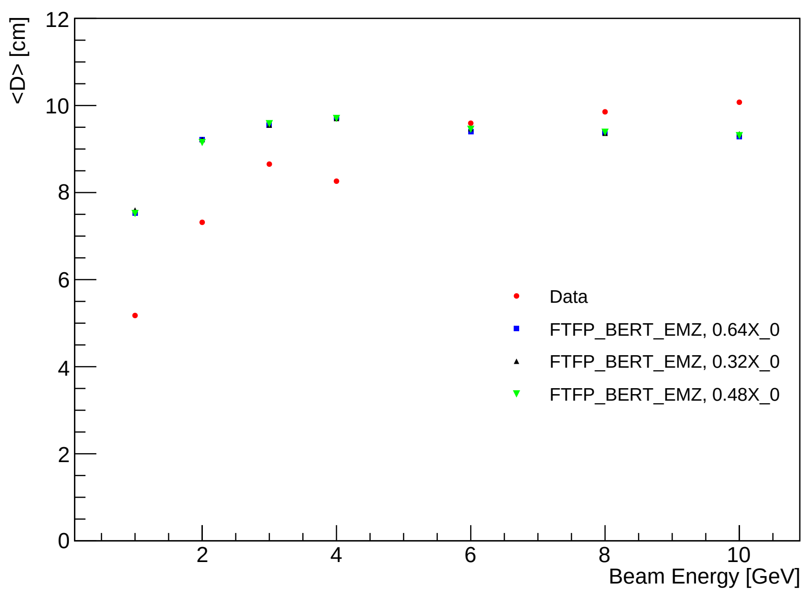


**Figure 7.19:** Mean radial dispersion of hits for pions. Different physics lists FTFP-BERT-EMZ with 0.64 (blue), 0.32 (black), and 0.48 (green) $X_0$ upstream material are shown. Data is plotted in red.

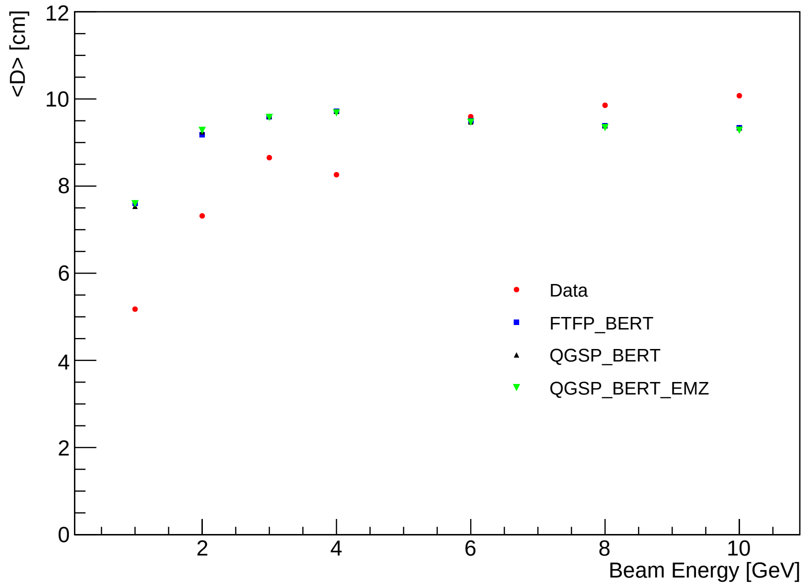


**Figure 7.20:** Mean radial dispersion of hits for pions. Different physics lists FTFP-BERT (blue), QGSP-BERT (black), and QGSP-BERT-EMZ (green) with 0.64 $X_0$ upstream material are shown. Data is plotted in red.

## 7.4 Density of Hits

The number of hits within a $3 \times 3 \times 3$ pad volume surrounding each hit defines the density at that hit. Figure 7.21 and Figure 7.22 present the hit density distributions for 3 to 10 GeV pions in both data and simulation. Good agreement is observed at higher energies (6, 8, and 10 GeV), but not at 3 and 4 GeV. In the simulation, the lower energy tail rises, a behavior not seen in the data. The simulation shows a higher hit density compared to the data; this result was anticipated based on the comparison of mean radius and dispersion of hits (see Figure 7.17 and Figure 7.19), as these metrics are correlated.

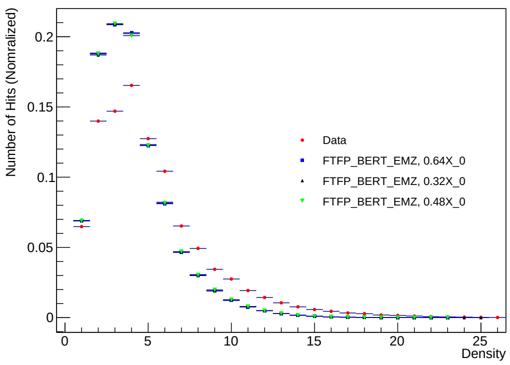


**(a)** Density distribution of 3 GeV pions

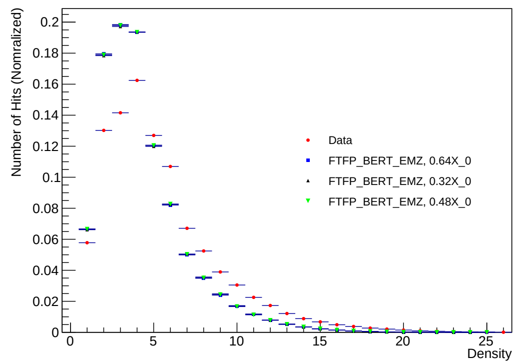


**(b)** Density distribution of 4 GeV pions

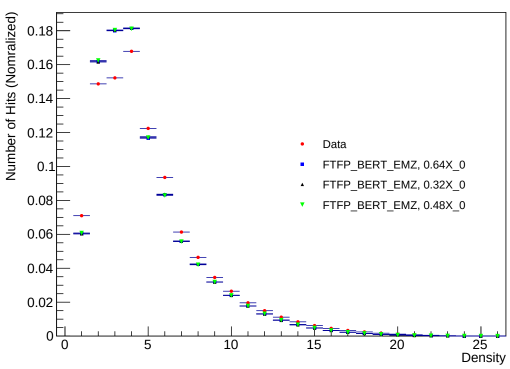


**(c)** Density distribution of 6 GeV pions

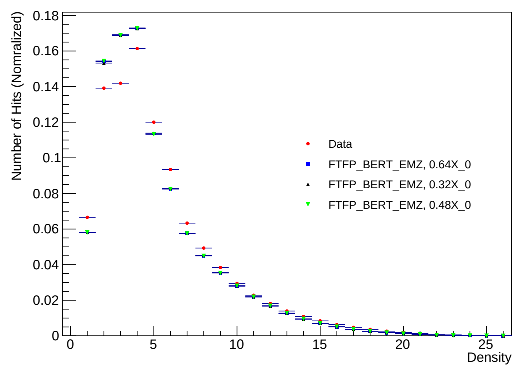


**(d)** Density distribution of 8 GeV pions

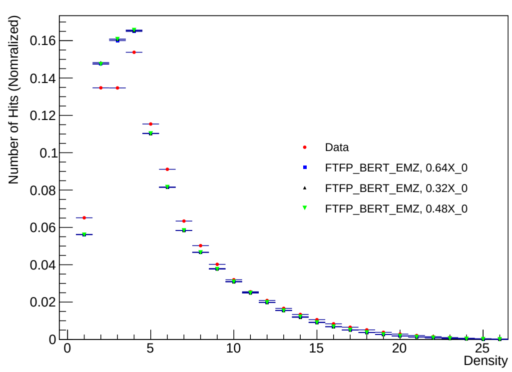


**(e)** Density distribution of 10 GeV pions

**Figure 7.21:** Density distribution for data (red) and simulation using different physics lists: FTFP-BERT-EMZ with 0.64 (blue), 0.32 (black), and 0.48 (green) $X_0$ upstream material.

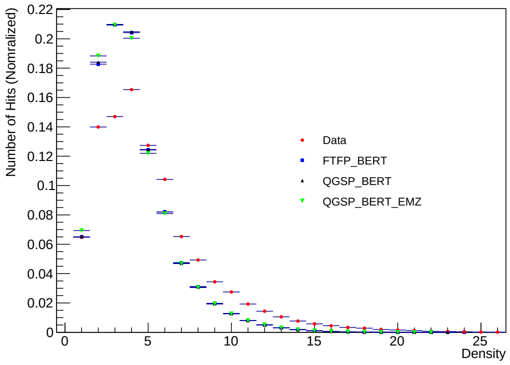


**(a)** Density distribution of 3 GeV pions

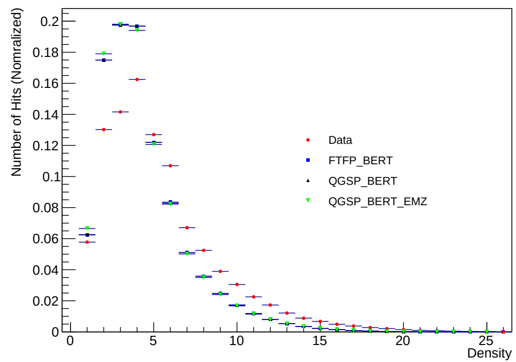


**(b)** Density distribution of 4 GeV pions

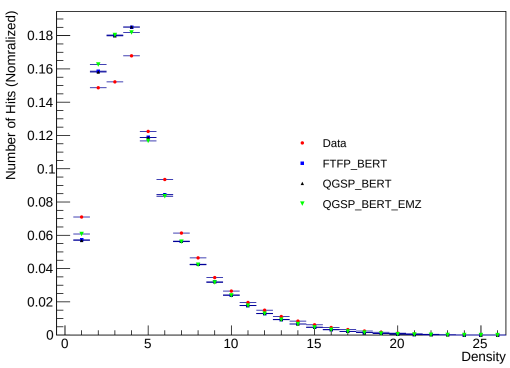


**(c)** Density distribution of 6 GeV pions

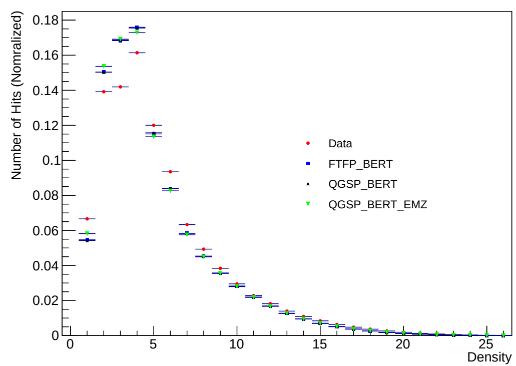


**(d)** Density distribution of 8 GeV pions

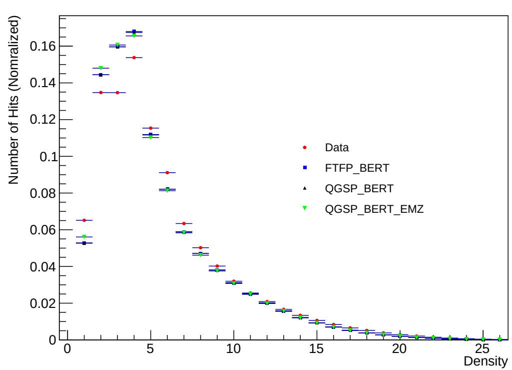


**(e)** Density distribution of 10 GeV pions

**Figure 7.22:** Density distribution for data (red) and simulation using different physics lists: FTFP-BERT (blue), QGSP-BERT (black), and QGSP-BERT-EMZ (green) with 0.64 $X_0$ upstream material.

## 7.5 Systematic Errors

The following section elaborates on the systematic errors linked to pion measurements.

- Figure 6.5 showed the hit distribution of a 6 GeV pion before and after the calibration is applied. The response shifts to the right post-calibration. The systematic error for measurements at each energy level was determined as half the average difference between results obtained before and after applying the calibration.

- Systematic errors also arise from the pion selection process, which is based on the interaction layer. Both data and simulation require at least 4 hits in five or more consecutive layers. Since the equalization is built into the simulation, selection criteria differ between data and simulation. To estimate the systematic error from this selection effect, the required number of consecutive layers in the data was varied between 4 to 6. The average difference was taken as a systematic error. Figure 7.23 illustrates a longitudinal shower profile of 10 GeV pions, with variation in the number of consecutive layers required for identifying pions.

- In the data samples, some ASICs were non-responsive, creating dead areas for recording hits. These dead areas, identified and applied to simulations, account for less than 1% of pads across the entire detector.

Another source of systematic errors is the use of the Novosibirsk function for fitting the hits and energy distributions in Chapter 7. Systematic uncertainty can be analyzed

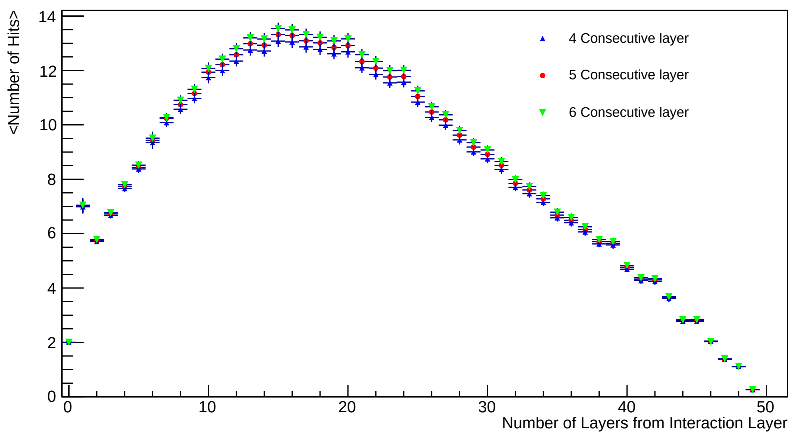


**Figure 7.23:** Longitudinal shower as a function of layer for 10 GeV pions, in red is shown the standard cut, in Blue less, and black more consecutive layers with hits are required.

by adjusting the range of the fits, performing the analysis for each variation, and then extrapolating the results to achieve zero contamination. Table 7.3 summarizes the different uncertainties for selected measurements.

| | **Systematic error** | **Longitudinal Profiles** | **Transverse Profile** | **Slope of Mean Response** |
|---|---|---|---|---|
| **Data** | Calibration uncertainty | ±5.7% | ±1.6% | ±3.1% |
| | Interaction layer | ±0.2% | ±1.2% | ±1.3% |
| | Fits | ±0.2% | ±0.05% | ±0.9% |
| **Simulation** | Statistical uncertainties | ±4% | ±1% | ±2% |
| | Dead ASICS | ±0.2% | ±0.3% | ±0.2% |
| | Fits | ±0.1% | ±0.05% | ±0.9% |

**Table 7.3:** Systematic errors for both the data and simulation given as an example for 6 GeV pion.

# Chapter 8

# Discussion and Conclusion

The Digital Hadronic Calorimeter (DHCAL) with minimal absorber collected data at Fermilab in November 2011. Despite employing an equalization method to address performance discrepancies among the Resistive Plate Chamber (RPC), more sophisticated calibration methods and simulations are necessary. The pion energy resolution is significantly affected by leakage and interference from positron and muon components. Pion showers, which are distributed across the entire detector with minimal absorber layers, allow for detailed comparisons with simulations.

Issues were identified in the tuning process of the simulation. Various upstream materials and physics lists were used for comparison with the data. Generally, differences between models were minor compared to the discrepancies between the data and simulation. The primary reasons for the lack of improvement in hadronic energy resolution are low energy and limited statistics. Further development of sophisticated programs for simulating RPC responses is required. The density information of hits can be utilized as software compensation to linearize responses.

The Min-DHCAL is ideal for validating current hadronic models. More data and extensive work are needed to optimize the tuning process, which would provide a more definitive assessment of the performance of different hadronic showers. This, in turn, would offer crucial feedback for developers of the GEANT4 simulation software.

# Bibliography


[1] B. Freund, “The Digital Hadron Calorimeter: Analysis of the November 2011 Fermilab Data,” Master’s thesis, McGill University, Department of Physics, Montreal, Quebec, Canada, July 2015. A thesis submitted in partial fulfillment of the requirements for the M.Sc. degree.

[2] J. J. Thomson, “XL. Cathode Rays,” *The London, Edinburgh, and Dublin Philosophical Magazine and Journal of Science*, vol. 44, no. 269, pp. 293–316, 1897.

[3] E. Rutherford, “LXXIX. The scattering of  and  particles by matter and the structure of the atom,” *The London, Edinburgh, and Dublin Philosophical Magazine and Journal of Science*, vol. 21, no. 125, pp. 669–688, 1911.

[4] J. Chadwick, “Possible Existence of a Neutron,” *Nature*, vol. 129, p. 312, 1932. Published: 27 February 1932.

[5] D. J. Griffiths, *Introduction to Elementary Particles.* Wiley-VCH, 2nd ed., 2004.

[6] "Standard Model of Elementary Particles." `https://upload.wikimedia.org/wikipedia/commons/0/00/Standard_Model_of_Elementary_Particles.svg`. (accessed: 2024).

[7] A. O. Sushkov *et al.*, "New Experimental Limits on Non-Newtonian Forces in the Micrometer Range," *Physical Review Letters*, vol. 107, Oct. 2011.

[8] V. Barger, D. Marfatia, and K. L. Whisnant, *The Physics of Neutrinos*. Princeton: Princeton University Press, 2012.

[9] NASA Science: Astrophysics, "Dark Energy, Dark Matter." `https://science.nasa.gov/universe/dark-matter-dark-energy/`, June 5 2015. Accessed: 2024-06-10.

[10] W. R. Leo, *Techniques for Nuclear and Particle Physics Experiments*. Berlin, Heidelberg: Springer Berlin Heidelberg, 1994.

[11] C. Grupen and B. Schwartz, *Particle Detectors*. Cambridge University Press, 2nd ed., 2008.

[12] D. Groom and S. Klein, "Passage of Particles Through Matter," *LBNL*, 2019. Revised August 2019.

[13] C. W. Fabjan and F. Gianotti, "Calorimetry for particle physics," *REVIEWS OF MODERN PHYSICS*, vol. 75, October 2003. Published 15 October 2003.

[14] B. Bilki, J. Repond, and L. Xia, "Development of Imaging Calorimetry," August 2013.

[15] C. Adloff *et al.*, "Hadronic energy resolution of a highly granular scintillator-steel hadron calorimeter using software compensation techniques," *Journal of Instrumentation*, vol. 7, September 2012. Published 27 September 2012.

[16] M. A. Thomson, "Particle flow calorimetry and the PandoraPFA algorithm," *Nuclear Instruments and Methods in Physics Research, Section A: Accelerators, Spectrometers, Detectors and Associated Equipment*, vol. 611, no. 1, pp. 25–40, 2009.

[17] CALICE Collaboration, "CALICE Collaboration TWiki." `https://twiki.cern.ch/twiki/bin/view/CALICE/WebHome`. [Accessed: 2024-08-10].

[18] Fermilab Test Beam Facility, "Fermilab Test Beam Facility." `http://ftbf.fnal.gov`, 2024. Accessed: 2024-07-22.

[19] CERN, "Proton Synchrotron." `http://home.cern/about/accelerators/proton-synchrotron`, 2024. Accessed: 2024-07-22.

[20] CERN, "Super Proton Synchrotron." `http://home.cern/about/accelerators/super-proton-synchrotron`, 2024. Accessed: 2024-07-22.

[21] G. Drake, J. Repond, D. Underwood, and L. Xia, "Resistive Plate Chambers for hadron calorimetry: Tests with analog readout," *Argonne National Laboratory*, vol. 9700, pp. 1–12, April 2007.

[22] The CALICE Collaboration, "Construction of the Digital Hadron Calorimeter," 2012.

[23] The CALICE Collaboration, "Analysis of DHCAL Muon Data," Analysis Note CAN-030, CALICE Collaboration, March 2011.

[24] C. Adams *et al.*, "Design, construction and commissioning of the Digital Hadron Calorimeter—DHCAL," *Journal of Instrumentation*, vol. 11, p. P07007, jul 2016.

[25] B. Bilki *et al.*, "Tests of a novel design of Resistive Plate Chambers," *Journal of Instrumentation*, vol. 10, p. P05003, may 2015.

[26] C. Adams *et al.*, "Design, Construction and Testing of the Digital Hadron Calorimeter (DHCAL) Electronics," 2016.

[27] "Design, Construction and Commissioning of a Technological Prototype of a Highly Granular SiPM-on-tile Scintillator-Steel Hadronic Calorimeter, author=The CALICE Collaboration," *CALICE Public Notes*, no. 003, 2022.

[28] B. Freund *et al.*, "DHCAL with minimal absorber: measurements with positrons," *Journal of Instrumentation*, vol. 11, p. P05008–P05008, May 2016.

[29] K. Francis, "Construction of the DHCAL," in *TIPP 2011 - Technology and Instrumentation in Particle Physics 2011*, (9700 S. Cass Avenue, Argonne, IL 60439, U.S.A.), Argonne National Laboratory, 2011. On behalf of the CALICE collaboration.

[30] The CALICE Collaboration, "The DHCAL Results from Fermilab Beam Tests: Calibration," May 2013. CALICE Analysis Note CAN-042.

[31] B. B. et al., "Environmental dependence of the performance of Resistive Plate Chambers," *JINST*, vol. 5, p. P02007, 2010.

[32] B. Bilki, "The CALICE digital hadron calorimeter: calibration and response to pions and positrons, publisher = IOP Publishing," vol. 587 of *Journal of Physics: Conference Series*, 2015. On behalf of the CALICE Collaboration.

[33] S. Agostinelli *et al.*, "Geant4—a simulation toolkit," *Nuclear Instruments and Methods in Physics Research Section A: Accelerators, Spectrometers, Detectors and Associated Equipment*, vol. 506, no. 3, pp. 250–303, 2003.

[34] J. Allison *et al.*, "GEANT4 developments and applications," *IEEE Transactions on Nuclear Science*, vol. 53, no. 1, pp. 270–278, 2006.

[35] B. Bilki, "Private communication," 2024. Personal communication, July 19, 2024.

[36] B. Bilki *et al.*, "Measurement of positron showers with a Digital Hadron Calorimeter," *Journal of Instrumentation*, vol. 4, p. P04006, 2009.

[37] T. C. Collaboration, "Analysis of Testbeam Data of the Highly Granular RPC-Steel CALICE Digital Hadron Calorimeter and Validation of GEANT4 Monte Carlo Models," *arXiv*, vol. 1901.08818v1, Jan 2019.

[38] A. Dotti, “Simulation of Showers with GEANT4,” (Stanford, California, USA), SLAC National Accelerator Laboratory, 2013. On behalf of the Geant4 Hadronic and Electromagnetic Working Groups.

[39] GEANT4 Collaboration, *Physics Reference Manual*, 2024. Accessed: 2024-08-29.

[40] C. Adloff *et al.*, “Validation of GEANT4 Monte Carlo models with a highly granular scintillator-steel hadron calorimeter,” *Journal of Instrumentation*, vol. 8, p. P07005, 2013.

[41] D. H. Wright, “Improving the Medium and Low Energy Physics Models in GEANT4,” in *International Conference on Calorimetry for the High Energy Frontier*, pp. 254–259, 2013.

[42] H. Ikeda *et al.*, “A detailed test of the CsI(Tl) calorimeter for BELLE with photon beams of energy between 20-MeV and 5.4-GeV,” *Nucl. Instrum. Meth. A*, vol. 441, pp. 401–426, 2000.

[43] P. Amaral *et al.*, “Hadronic Shower Development in Iron-Scintillator Tile Calorimetry,” *CERN-EP/99*, 1999.